Arctic sea ice anomalies during the MOSAiC winter 2019/20

Klaus Dethloff[1], Wieslaw Maslowski[2], Stefan Hendricks[3], Younjoo Lee[2], Helge F. Goessling[3], Thomas Krumpen[3], Christian Haas[3], Dörthe Handorf[1], Robert Ricker[3], Vladimir Bessonov[4], John J. Cassano[5], Jaclyn Clement Kinney[2], Robert Osinski[6], Markus Rex[1], Annette Rinke[1], Julia Sokolova[4], Anja Sommerfeld[1]

[1] Alfred Wegener Institute, Helmholtz Centre for Polar and Marine Research, Telegrafenberg A45, 14473 Potsdam, Germany
[2] Department of Oceanography, Graduate School of Engineering and Applied Sciences, Naval Postgraduate School, Monterey, CA 93943, US[3] Alfred Wegener Institute, Helmholtz Centre for Polar and Marine Research, Am Handelshafen 12, 27570 Bremerhaven, Germany
[4] Arctic and Antarctic Research Institute, Center Ice and Hydrometeorological Information, Bering Street 38, St. Petersburg, Russia
[5] Cooperative Institute for Research in Environmental Sciences, National Snow and Ice Data Center and Department of Atmospheric and Oceanic Sciences, University of Colorado, Boulder, US
[6] Institute of Oceanology, Polish Academy of Sciences, Sopot 81712, Poland

Correspondence to: Klaus Dethloff (Klaus.Dethloff@awi.de) and Wieslaw Maslowski (maslowsk@nps.edu)

Abstract. As the Multidisciplinary drifting Observatory for the Study of Arctic Climate (MOSAiC) project went into effect during the winter of 2019/2020, the Arctic Oscillation (AO) has experienced some of the largest shifts from a highly negative index in November 2019 to an extremely positive index during January-February-March (JFM) 2020. Here we analyse the sea ice thickness (SIT) distribution based on CryoSat-2/SMOS satellite data augmented with results from the hindcast simulation by the fully coupled Regional Arctic System Model (RASM) for the time period from November 2019 through March 2020. A notable result of the positive AO phase during JFM 2020 were large SIT anomalies, up to 1.3 m, which emerged in the Barents-Sea (BS), along the northeastern Canadian coast and in parts of the central Arctic Ocean. These anomalies appear to be driven by nonlinear interactions between thermodynamic and dynamic processes. In particular, in the Barents- and Kara Seas (BKS) they are a result of an enhanced ice growth connected with the colder temperature anomalies and the consequence of intensified atmospheric-driven sea ice transport and deformations (i.e. divergence and shear) in this area. Low-pressure anomalies, which developed over the Eastern Arctic during JFM 2020, increased northerly winds from the cold Arctic Ocean to the BS and accelerated the southward drift of the MOSAiC ice floe. The satellite-derived and model-simulated sea ice velocity anomalies, which compared well during JFM 2020, indicate a strong acceleration of the Transpolar Drift relative to the mean for the past decade, with intensified speeds up to 6 km/day. As a consequence, sea ice transport and deformations driven by atmospheric wind forcing accounted for bulk of SIT anomalies, especially in January and February 2020. The unusual AO shift and the related sea ice anomalies during the MOSAiC winter 2019/20 are within the range of simulated states in the forecast ensemble. RASM intra-annual ensemble forecast simulations, forced with different atmospheric boundary conditions from November 1, 2019 through April 30, 2020, show a pronounced internally generated variability in the sea ice volume. A comparison of the respective SIT distribution and turbulent heat fluxes during the positive AO phase in JFM 2020 and the negative AO phase in JFM 2010 further corroborates the conclusion, that winter sea ice conditions of the Arctic Ocean can be significantly altered by AO variability.

1 Introduction

The temporal evolution of Arctic sea ice thickness distribution is the result of complex and highly variable interactions within the pack ice and its interactions with atmospheric and oceanic processes (e.g. *Belter et al. 2020).* Since the late 1970s, remotely sensed measurements have provided Arctic-wide information about its changing sea ice cover (https://nsidc.org/cryosphere/seaice/study/remote_sensing.html), which motivated the development of new satellite products (*Zwally et al. 2002; Stern and Moritz, 2002; Spreen et al. 2008; Tilling et al. 2018; Neumann et al. 2019*) as well as regionally-focused coupled Arctic system models and sea ice predictions systems (e.g. *Dorn et al. 2007; Dorn et al., 2009; Maslowski et al. 2012*), to address stakeholder needs for information related to shipping, resource extraction and climate monitoring. Oceanic heat inflows into the Arctic Ocean, through the Bering Strait from the Pacific side and through the Barents Sea (BS) and Fram Strait from the Atlantic side, and sea ice impacts on the vertical structure of the upper halocline downstream. *Schlichtholz (2019)* demonstrated, that more than 80% of the variance of the leading variability mode in the winter Arctic sea ice concentration from 1981–2018, with main centers of action appearing in the BS region, can be explained by the preceding summertime temperature anomalies of Atlantic water inflow from the Norwegian Sea. The variability of Arctic sea ice distribution, drift and deformation is connected to atmospheric circulation patterns and cyclonic systems with impacts on the dynamical ice redistribution and thermo-dynamical sea ice growth- and melt. Wind patterns affect the BS and Barents-Kara Seas (BKS) ice variability through momentum transfer, advection of cold and dry or warm and humid air, forcing of warm Atlantic water inflow into the BS and by increased or decreased turbulent surface heat fluxes.

Since the BS is a shallow marginal sea, the wind-driven together with tidal mixing effectively remove the bulk of Atlantic water heat to the atmosphere and only a small amount of the heat enters the deep Arctic basin (*Gammelsrod et al. 2009; Onarheim et al. 2015).* Therefore, oceanic heat convergence and atmospheric winds appear as the main drivers of the BS ice cover. Northerly winds influence sea ice advection mainly in winter during strong wind events and processes related to large-scale atmospheric circulation patterns*,* cyclonic activity, the length of the freezing season, and the remaining sea ice volume after the summer melt season are of also of importance for sea ice variability in winter.

The observed decline of Arctic sea ice was identified as a main contributor to changes in the large-scale Arctic Oscillation (AO) pattern and mid-latitude climate changes during winter, e. g. *Cohen et al. (2014).* The origin of AO changes between positive and negative phases has been attributed to declining sea ice in Arctic regions (*Screen et al., 2013*), planetary-synoptic circulation adjustment processes (*Dethloff et al. 2006; Sokolova et al., 2017*), changes in Siberian snow cover (*Cohen et al., 2012*), weakening and warming of the stratospheric polar vortex (*Kim et al., 2014*), natural variability (*McCusker et al., 2016*) and anthropogenic greenhouse gases (*Johannessen et al., 2004*). As pointed out by *Ding et al. (2019),* Arctic sea ice changes non-uniformly under the influence of multiple internal or external factors.

The BS has been considered as a key region for the observed fast Arctic climate changes due to intense air-sea interaction as pointed out by *Smedsrud et al. (2013)* and anomalous turbulent heat fluxes by impacting the AO winter phase via mediation of surface heat fluxes at the ocean-atmosphere interface (*Liptak and Strong 2014).* An inflow of warm Atlantic water influences the sea ice cover in the BS and its decline there has been connected to a northward shift of the Gulf Stream front *(Sato et al. (2014).* Despite many model efforts, so far no consensus has been reached with regard to the connection of Arctic sea ice reductions with AO phase changes, with some studies pointing to positive AO changes *(e.g. Orsolini et al. 2014)* while others reasoning for negative changes *(Peings and Magnusdottir 2014). Nakamura et al. (2015)* showed, that a stationary Rossby wave response to sea ice reduction in the BS might introduce anomalous circulation pattern similar to the negative AO phase and tropospheric cyclonic anomalies over Siberia, formed by the Rossby wave response to a wave source in the BKS region. *Nie et al. (2019)* emphasised the role of initial stratospheric conditions and wind anomalies in November. Westerly wind anomalies result in positive AO winter phases and the reverse happens for easterly initial anomalies. *Kolstad and Screen (2019)* showed that the correlation between autumn BKS ice and the winter North Atlantic Oscillation is non-stationary and contains considerable decadal variability. They argued that recent observed high correlation can be explained purely by internal

variability, a view supported by *Blackport et al. (2019). Gong et al. (2020)* emphasized an Arctic wave train propagating from the subtropics through mid-latitudes into the Arctic and back into mid-latitudes, which is recharged and amplified in the Arctic

90 through anomalous surface heat flux anomalies over the Greenland Sea and the BKS. The processes responsible for the observed sea ice loss in the Arctic are influenced by coupled, nonlinear atmosphere-ocean-sea ice feedbacks in different regions of the Arctic Ocean basin as discussed by *Bushuk et al. (2019)*. The two-way interaction between ocean, sea ice and atmosphere impacts via surface turbulent heat fluxes on the lower troposphere, which feeds back with changed thermo-dynamical ice growth conditions and atmospheric wind stress forcing. *Zhao et al. (2019)* described positive and negative feedbacks related

95 to the AO revealed by surface heat fluxes in the Nordic Seas based on NCEP reanalysis data.

Platov et al. (2020) noted three modes of the surface wind forcing on the Arctic sea ice. The first, oceanic mode, is associated with the cyclonic or anticyclonic type of circulation in the Arctic Ocean as discussed by *Proshutinsky and Johnson (1997)*. The second, dipole mode, accelerates or slows down the Transpolar Drift. The third, Atlantic mode, weakens or intensifies the cyclonic gyre in the northern Northern Atlantic, corresponding to the atlantification trends (*Barton et al., 2018*)) in the BKS.

100 *Trofinov et al. (2020)* described temperature decrease of more than 1°C in the inflowing Atlantic water to the BS since 2015 and argue that lower temperatures, in combination with reduced inflow during winter have caused the increases in BS winter sea ice observed in recent years. Sea surface temperature averaged over the southern BS dropped significantly in 2019 and its annual mean value was the lowest since 2011. In the Eurasian Basin of the Arctic Ocean, *Polyakov et al. (2020)* noticed a weakening of the ocean stratification over the halocline, which isolates intermediate depth Atlantic water from the surface

105 mixed layer. The oceanic turbulent heat fluxes increased and were greater than 10 W/m^2 for the winters of 2016–18, with significant impacts on sea ice loss in this region. These oceanic changes have the potential to increase baroclinic instability in the early Arctic winter troposphere, which impacts on synoptic scale structures in autumn and planetary waves in late winter (*Jaiser et al. 2012*), increases Arctic storm activity and play an important role for meridional heat transport into the BKS (*Long and Perrie, 2017*).

110 The connection between sea ice and atmospheric circulation is critical for understanding the abrupt circulation changes, which the atmosphere and sea ice experienced during the winter 2019/20. The leading atmospheric variability pattern moved from a below-average AO negative phase in November 2019 to a highly positive and persistent AO phase during January-March 2020. The positive AO phase in the Arctic troposphere was accompanied by cold surface temperatures and enhanced near surface wind anomalies, and connected with an exceptionally strong and persistent cold stratospheric polar vortex (*Lawrence*

115 *et al. 2020*). During the MOSAiC winter 2019/20, the tropospheric wave activity and wave forcing was weak and the stratospheric vortex developed an unusual configuration, which reflected planetary waves back into the troposphere and impacted the lower atmospheric circulation. The distribution and transport of Arctic sea ice is driven by near surface wind fields, dominated in winter by the Beaufort High, which yields an anti-cyclonic sea ice drift within the Beaufort Gyre. Its northern branch, the Transpolar Drift, moves sea ice from the Siberian coast across the deep basin toward the Fram Strait and

120 the Nordic Seas. The positive (negative) AO is characterized by low (high) sea level pressure anomalies over the Arctic that lead to cyclonic (anti-cyclonic) atmospheric circulation anomalies (*Armitage et al. 2018*), a contracted (expanded) Beaufort Gyre circulation (*Kwok et al. 2013*) and respective shifts of the Transpolar Drift. *Proshutinsky and Johnson (1997)* discussed the alternating appearance of cyclonic and anti-cyclonic circulation regimes of the wind driven Arctic Ocean. During cyclonic regimes, low sea-level atmospheric pressure dominated over the Arctic Ocean driving sea ice and the upper ocean counter

125 clockwise whereas during anti-cyclonic circulation regimes, high sea level pressure dominated with clockwise circulation. During the winter 2019/20, the international research project MOSAiC (Multidisciplinary drifting Observatory for the Study of Arctic Climate) used the research icebreaker "Polarstern" *(Polarstern: Alfred-Wegener-Institut Helmholtz-Zentrum für Polar- und Meeresforschung. (2017)),* operated by the German Alfred Wegener Institute, Helmholtz Centre for Polar and Marine Research, was docked to a stable sea ice floe north of the Laptev Sea in October 2019. Following the drift pattern

130 established by the Russian North Pole drifting stations since 1937 (*AARI 1993, Frolov et al., 2005*) the ice floe traveled from

October 2019 until July 2020 with the Transpolar Drift toward the Fram Strait. *Krumpen et al. (2020)* described the origin and initial conditions of sea ice at the start of the MOSAiC experiment. Their results showed that the sea ice within 40 km of the MOSAiC Central Observatory was younger and thinner than surrounding ice and it was formed in a polynya event north of the New Siberian Islands at the beginning of December 2018. They determined, that those sea ice conditions were due to the

135   interplay between a high ice export in the late winter preceding MOSAiC and high air temperatures during the following summer, which yielded the longest ice-free summer period of 93 days over the Siberian shelf seas since the beginning of the records. The exchange of RV "Polarstern" crew and researchers in February/March 2020, carried out for the MOSAiC project by the Russian icebreaker "Kapitan Dranitzyn" was significantly influenced and delayed by heavy sea ice conditions along the MOSAiC drift in the Arctic Ocean and in the BKS. Along the "Kapitan Dranitzyn" cruise track, in situ sea ice thickness

140   measurements were carried out.

Here we diagnose and focus on the regional processes in the Arctic at the ocean-sea ice interface with the atmospheric conditions, thermodynamic sea ice growth and dynamical sea ice divergence, convergence and ice shear processes during the winter 2019/20. Although an investigation of the highly nonlinear mechanisms for the AO changes is beyond the scope of this paper, the positive AO phase during January-March (JFM) 2020 is essential for the observed sea ice changes, as regional

145   feedbacks are a function of the background climate state. We based our analysis on satellite derived sea ice thickness data and output of the hindcast simulation using the fully coupled Regional Arctic System Model (RASM), with AO phase nudged above 500 hPa, to examine the spectrum of nonlinear process-driven interactions between the Arctic Ocean, sea ice and the atmosphere. As a regional climate model forced along the boundaries with realistic global atmospheric reanalysis, such as the National Centers for Environmental Predictions (NCEP) Coupled Forecast System (CFS) Reanalysis (CFSR), RASM offers a

150   unique capability to reproduce the observed natural environmental conditions in place and time. Given such capabilities, we (i) evaluate RASM skill in reproducing the sea ice thickness distribution from the CryoSat-2/SMOS satellite data from November 2019 until March 2020, (ii) diagnose the evolution of sea ice, (iii) investigate the mechanisms of and the interplay between the thermodynamic growth and dynamic sea ice processes under the influence of a positive AO phase. The synthesis of sea ice thickness distribution and growth simulated by RASM with the CryoSat-2/SMOS data, allows for improved

155   understanding of the regional drivers of sea ice changes within the positive AO variability pattern in winter 2019/20 determined from the European Reanalysis data ERA-5. In chapter 2 we provide details of the used satellite data and the model setup for the hindcast and forecast simulations. Chapter 3 presents results on the AO phase changes from November 2019 until March 2020 based on ERA-5 data, sea ice thickness estimates from the CryoSat-2/SMOS and the RASM hindcast, the evaluation of RASM simulations, the thermodynamic and dynamic contributions to the observed sea ice anomalies, and changes in the

160   Transpolar Drift. We end this chapter with results from the RASM ensemble forecasts to quantify the strength of internal variability driven by regional processes within the Arctic climate system and a comparison of RASM sea ice conditions and turbulent surface heat fluxes between the AO positive 2019/2020 and AO negative 2009/2010 winters.

2 Data and model set up

The algorithms and methods used for the satellite retrieval of sea ice thickness products, the RASM model and the ERA5 data

165   will be described in the following section. Monthly gridded sea-ice thickness information from remote sensing is based on the ESA CryoSat-2/SMOS Level-4 sea ice thickness data set, produced and disseminated by the Alfred Wegener Institute, Helmholtz Centre for Polar and Marine Research. The data is based on merging two independent sea-ice thickness data sets from CryoSat-2 (*Hendricks et al., 2020*) and SMOS (*Tian-Kunze et al., 2014*) by optimal interpolation (*Ricker et al., 2017*), resulting in gap-less sea-ice thickness information in the complete northern hemisphere with sensitivity across the full sea-ice

170   thickness spectrum. Here, we use the product version 2.02 (*Ricker, 2019*), which is available as daily-updated gridded product with a moving observation time window of seven days between October 15 and April 15 of winter seasons since November 2010. We compute monthly sea-ice thickness fields by attributing the reference time, defined as the center time in the seven-

day period, to the calendar month and average all thickness fields within one calendar month respectively. We also compute the sea-ice thickness anomaly, the difference of a monthly sea-ice thickness field, to the average conditions of this month in
175 the CryoSat-2/SMOS data record (2010-2019) both as a difference in meters and the relative difference as a percentage of average sea-ice thickness. In addition, we use continuous, along-track, ship-based electromagnetic ice thickness measurements that were carried out on board of the Russian icebreaker "Kapitan Dranitzyn" during the second resupply voyage of RV Polarstern between 6 and 14 March 2020. Detailed information about the measurements can be found in *Haas (1998)* and *Haas et al. (1999)*.

180 Regional climate models offer exceptional spatio-temporal coverage and insights into processes and feedbacks not fully resolved in global Earth System models. They form part of a model hierarchy important for improving regional climate predictions and projections. The Regional Arctic System Model (RASM) has been developed and used to better understand the past and present operation of the Arctic climate system at process scales and to predict its change at time scales from days up to decades, see *Maslowski et al. (2012), Cassano et al. (2017),* and *Roberts et al. (2018)*. RASM is a high-resolution, limited-area,
185 fully coupled climate model, consisting of atmosphere, ocean, sea ice, marine biogeochemistry, land hydrology and river routing components. The model domain is pan-Arctic, as it covers the entire marine cryosphere of the Northern Hemisphere, terrestrial drainage to the Arctic Ocean and its major atmospheric inflow and outflow pathways, with optimal extension into the North Pacific/Atlantic to model the passage of cyclones into the Arctic. Its pan-Arctic atmosphere and land component domains are identical and configured on a 50-km grid. The ocean and sea ice components use a 1/12° (~9.3 km, i.e. eddy-permitting) grid in
190 the horizontal direction and 45 vertical layers. The regional model hindcast simulation was set up in the following way. The initial boundary conditions in the ocean and sea ice were derived from the stand-alone ocean and sea ice model 32-year (1948-1979) spin-up forced with the Coordinated Ocean-ice Reference Experiments phase II (CORE II, *Large and Yeager, 2008*) inter-annual atmospheric reanalysis. The ocean lateral boundary conditions were derived from the monthly University of Washington Polar Science Center Hydrographic Climatology version 3.0 (PHC3.0, *Steele et al., 2001*). The atmospheric lateral
195 boundary forcing as well as the grid point nudging of temperature and winds from 500 hPa to 10 hPa were based on 6-hourly NCEP CFSR data for 1979 through March 2011 and CFS version 2 (CFSv2) analyses afterwards. The hindcast simulation used here started in September 1979 and has been updated through 2020.

The RASM ensemble forecast simulations have been produced monthly since January 2019, with each ensemble (consisting of 28-31 members) initialized on the 1st of each month and run for 6 months to produce intra-annual forecasts of the Arctic
200 environment (https://nps.edu/web/rasm/predictions). The ensemble forecasts used here were initialized on 1 November 2019 and finished by 1 May 2020. These forecasts use global output from the NCEP CFSv2 operational 9-month forecasts initialized at 0000 each day of the preceding month, resulting with the November 2019 ensemble consisting of 30 members.

For additional atmospheric analysis, ERA5 data over the Arctic region, described by *Hersbach and Dee (2016)* were used. ERA5 has several improvements compared to ERA-I as a result of higher temporal and spatial resolutions and more consistent
205 sea surface temperature and ice concentrations.

3. Results

3.1 Sea ice thickness distributions in November 2019 and January-March 2020

3.1.1. Atmospheric circulation and AO phase

210 The AO index is the leading pattern of the mean height anomalies at the surface, and a positive AO index means a lower than normal pressure in the Arctic and higher pressure outside. Figure 1 presents daily values of the AO index in mean sea level pressure (SLP) based on ERA-5 from October 2019 until May 2020 with 7-day running mean (red line) and the spatial AO pattern. The pattern of the AO was defined as the leading mode of Empirical Orthogonal Function analysis of monthly mean SLP during the 1979-2000 period. The daily AO indices used for the shown time series and the probability density functions
215 (PDFs) displayed in Figure S1, have been obtained by projecting daily SLP data from 1979 to May 2020 onto this AO pattern.

Figure 1 indicates the unusual shift from a negative phase in November to the positive AO phase in January, February and March 2020. Figure S1 presents the PDFs of the AO indices for November and January-March (JFM) from 1979 until 2018/2019 (gray) in comparison to November 2019 (blue) and JFM 2020 (blue) with the prevailing positive AO-index in 2020. Figure 2 displays the SLP anomaly and the 2 m temperature anomaly for November 2019 and January 2020 and the SLP

220   anomalies for February and March 2020 compared to the mean for 2010-2019 based on ERA-5 data. During November the negative AO phase occurs with higher pressure anomaly over most regions of the Arctic Ocean and relatively warm temperatures in the Beaufort and Siberian Seas. This circulation is connected with atmospheric 10 m winds from the south-west of Greenland and warm air masses inflow into the Western Arctic. During January 2020 a low-pressure anomaly developed over the Eastern Arctic, whereas over the Western Arctic a high-pressure anomaly existed. This atmospheric flow

225   configuration induced strong northerly winds from the cold Arctic Ocean to the BS and accelerated the southward drift of the MOSAiC ice floe in the Transpolar Drift. A regional cold temperature anomaly developed in the northern part of BS. In February 2020 the low-pressure system stayed over the BKS and adjacent land regions and pushed sea ice into the BS, whereas the Kara Sea experienced southerly winds and thus warm anomalies. In March the low-pressure anomaly was located north of the Laptev Sea, inducing westerly wind anomalies following Arctic cyclone tracks in the BKS and keeping the cold air in the

230   Arctic.

3.1.2 Sea ice thickness and extent

The regional distribution of sea ice thickness and anomalies compared to average conditions (2010-2019) in the data record based on CryoSat-2/SMOS satellite data analysis for November 2019, January, February and March 2020 are displayed in

235   Figure 3. They show a regionally varying pattern of positive and negative sea ice anomalies. In November 2019 positive thickness anomalies occur in the Beaufort Sea, BS and northeast of Spitsbergen. At the Bering Strait a negative ice anomaly exists. In January 2020 a pronounced ice anomaly developed in the BKS, which persisted with regional changes in the Kara Sea through February into March 2020, when sea ice thickness increased west of Spitsbergen. Positive ice anomalies developed at the Bering Strait and the Canadian coast. In relative terms, the anomaly in the BKS is more significant, as it almost doubled

240   the thickness in the first-year ice region as seen in relative sea-ice thickness anomaly fields in the third column of Figure 3. November 2019 was a month with pronounced negative AO phase, whereas the months JFM 2020 were a period with the strong positive AO phase. Figure 3 clearly indicates enhanced sea ice anomalies in the BKS during JFM 2020. These sea ice anomalies occur at the same time as the persistent positive AO phase (Figure 1). To understand the underlying thermo-dynamical and dynamical contributions for the observed sea ice thickness evolution we will discuss simulation results from

245   the fully coupled RASM model.

3.2 Simulation of atmospheric and sea ice conditions in RASM
3.2.1 Model evaluation

Figure S2 presents the RASM-simulated atmospheric large-scale circulation exemplarily for January 2020 which compares

250   well to the SLP anomalies in the positive AO phase shown in Figure 1. The pronounced negative 2m temperature anomaly observed in the BS, seen in Figure 2, is also reproduced. The accurate simulation of this atmospheric circulation pattern is a result of grid point nudging of the atmosphere above 500 hPa in RASM to the AO phase. The SLP and temperature anomalies simulated by RASM (Figure S2) are associated with positive SIT anomalies in the BS and east of Spitsbergen presented in the second and third row of Figure 4. The simulated ice thickness anomalies for November 2019, January, February and March

255   2020 are in qualitative agreement with the satellite derived SIT anomalies for the same months displayed in Figure 3. The largest positive thickness anomalies, of up to 1.3 m, occur in the BS, along the north-eastern Canadian coast and in the central Arctic Ocean. In all other regions and especially over the Bering Strait and the Siberian Seas the sea ice is thinner than the 2010-2019 mean. Figure 4 additionally displays the positive SIT anomalies of the Arctic Ocean north-west of Greenland.

A more in-depth comparison of the SIT for November 2019 and JFM 2020 in Figure 5 indicates thicker ice stretching further
260   into the central Basin from Greenland in the CryoSat2/SMOS data compared to the RASM. In the BKS, the Laptev Seas and
the Bering Strait the RASM simulations indicates thicker sea ice in the range of up to 1 m compared to the satellite data. The
SIT simulations in RASM has been independently compared in a quality control with other coupled and uncoupled model
systems by *Roberts et al. (2018)* and are in good agreement with the limited observations. The differences in SIT could be
partly connected to the impact of surface roughness on the radar freeboards and the retrieval algorithms as discussed by *Landy*
265   *et al. (2020)*. Figure 5 relies on the usage of the 50% threshold method, which indicates a bit thicker ice in the central Arctic
compared to other retrieval algorithms and to the ICESat-2 estimates. *Landy et al. (2020)* estimated the principal source of
pan-Arctic SIT uncertainty due to variable ice surface roughness in the range of 20-30 %. Figure 5 shows in the right column
the high correlation between satellite and model estimated SIT in all considered months. Figure 6a displays the RASM bias
and root mean square differences and Figure 6b the standard deviations and correlations relative to CryoSat2/SMOS for each
270   month from November 2019 until March 2020 with respect to sea ice thickness. For all months the model simulations show a
high correlation above 0.7 and a low standard deviation to the satellite based SIT estimates. Table 1 compares the monthly
mean sea ice thickness, standard deviations, correlations, bias and root mean square difference between CryoSat-2/SMOS data
and the RASM hindcast simulations from November 2019 until March 2020. Overall the agreement is favorable with high
correlations between 0.84 and 0.86 and a low domain-averaged bias.

275

3.2.2 Interpretation of positive sea ice anomaly in the BS

The integrated sea ice growth anomalies of RASM are displayed in Figure 7 and indicate regionally varying ice growth over
the whole Arctic Ocean during polar night conditions. A closer look shows regions of enhanced ice growth, which in November
starts north-west of Greenland and along the sea ice border in the eastern Arctic. In January 2020 strong ice growth takes place
280   in the BKS and the Siberian Seas and the Bering Strait. In February the strongest ice growth anomalies occur over the Beaufort
and Chukchi Sea and in March over the mid-Arctic Ocean and parts of the BS and at the east coast of Greenland. In February
and March 2020 weaker sea ice growth is visible in the Laptev Sea, east of Greenland and the Davis Strait.

The ship-based ice thickness measurements as part of the MOSAiC resupply between 6 and 14 March 2020 indicated heavy
sea ice conditions between 84°N and 88°N in the BS. Mean daily, modal thicknesses are displayed in Figure 8 and compared
285   to the mean RASM simulations between 6 and 14 March 2020. The ship-based measurements ranged between 1.3 and 1.5 m
and are 0.3-0.5 m thinner than those from RASM. The ship based sea ice thickness is also 0.3-0.4 m thinner than what was
observed by ground-based measurements at the MOSAiC ice floe (not shown), where modal thicknesses between 1.7 and 1.8
m were measured. The bias of the ship-based measurements is likely a result of the frequent ramming operations of the ship
with little progress over the undisturbed heavy ice, which makes processing and filtering of the ship-based measurements
290   challenging. However, Figure 8 shows that RASM results would agree very well with observations, if ~0.4 m were added to
the ship-based data. Consequently, also the regional gradients in both data sets with thinner ice to the south are well described.
The movement of "Kapitan Dranitzyn" to "Polarstern" in the sectors of the BS of the Arctic basin in February and March 2020
was carried out in great distresses due to severe ice conditions. The most difficult parts of the route went through hummocked
thick first-year and second-year ice. The movement of the supply vessel slowed down significantly due to the absence of
295   extensive leads in the meridional direction and compression (especially in February on the way to Polarstern). Separate large
leads, which appeared after passing cyclones, were predominantly in the zonal direction. Compression weakening and local
fracture system allowed "Kapitan Dranitzyn" to move forward gradually to "Polarstern". Figure 9 indicates these sea ice leads
in the infrared channel of NOAA-20 satellite pictures on 5 March 2020 with a resolution of 375 m, which showed a clear zonal
orientation due to the low-pressure systems connected to the positive AO phase. Figure 9 also present a snapshot of the sea ice
300   divergence on 5 March 2020 from the RASM simulations, which shows a qualitatively-similar orientation of sea ice leads in
the BS and north of it.

Comparison of Figures 4 and 7 indicates, that positive sea ice growth anomalies in the BS occur in the region of positive thickness anomalies during JFM 2020. Therefore, enhanced sea ice thickness in the BS is partly a result of enhanced ice growth
305   connected with the colder temperature anomalies in this area as shown in Figures 2 and S2. But ice thickness anomalies are influenced by deformations, e.g. divergence/convergence and shear, commonly generated in response to strong and/or persistent winds. *Onarheim et al. (2015)* demonstrated, that the changes of atmospheric winds can explain 78% of the sea ice extent variance in the BS. This confirms, that oceanic heat transport and atmospheric winds are the main drivers of ice cover and their variabilities capture most of the sea ice variance in the BS. The exchange of momentum due to turbulent atmospheric
310   processes controls the sea ice motion. Divergence generates open water areas where new sea ice growth can occur. Convergence leads to the formation of pressure ridges and the SIT distribution a region can be often determined by the number and thickness of ice ridges.

Figure 10 displays the RASM-simulated ice convergence and divergence anomalies and the ice shear anomaly (both in percent/day) for the JFM 2020 mean compared to the JFM 2010-2019 mean, together with the transpolar drift in km/day
315   indicated by black arrows. The sea ice drift is a result of the near surface wind fields, which determines sea ice deformation. Sea ice momentum changes are a result of combined air-ice and ice-ocean stresses. Positive values in Figure 10 (left) describe positive ice convergence anomalies in the Fram-Strait and the BS between Spitsbergen and Novaya Zemlya. Positive ice divergence anomalies in Figure 10 (right) are present in the Fram-Strait and the west coast of Spitsbergen. This region also shows strong positive and negative values for the ice shear anomaly, which indicates the strong dynamical impact in the sea
320   ice formation and deformation in the BKS region. Reduced divergence, which corresponds to enhanced convergence appears in a belt between west Greenland and the Kara Sea. In areas close to the ice edge, positive ice shear values coincide with positive sea ice concentration anomalies, since more ice than usual exists there. The ice divergence anomalies are weaker and occur in the region of strongest sea ice growth, whereas ice shear processes due to wind stresses indicates here positive anomaly values. This leads to the conclusion, that the sea ice thickness anomalies in the BS region, where the negative temperature
325   anomalies occurred, are largely influenced and a result of wind stresses, which enable new ice growth or deformation. Atmospheric near surface wind advection impacts sea ice deformation and the 10 m wind vectors displayed in Figure 2 indicate strong wind components from the North in the region east of Spitsbergen. These wind components in the positive AO phase in JFM 2020 could be connected to an intensified and northward shifted Atlantic storm track as earlier discussed by *Serreze et al. (1997), Nie et al. (2008)* and *Inoue et al. (2012)*.
330

3.2.3. Transpolar sea ice drift

Figure 11 presents the model-simulated and satellite-derived sea ice velocity anomaly in km/day compared to the climate mean 2010-2019, computed from OSI-SAF low resolution sea ice motion data during January-March 2020 and indicates in both data sets a strong acceleration of the Transpolar Drift during the MOSAiC winter, with intensified speeds up to 6 km/day. This drift
335   is in general agreement with the 10 m winds displayed for January, February and March 2020 and the low-pressure anomalies both displayed in Figure 2. The centers of the persistent low-pressure systems over the Arctic Ocean corresponding to the positive AO phase, changed their positions during JFM 2020. In March the center moved toward Siberia, impacted the ice drift velocities in the BS region and contributed to the increased sea ice thickness. The low-pressure anomaly in March 2020 induced a stronger drift towards the BS. Sea ice growth in the BS was the combined effect of thermodynamic growth due to the colder
340   temperatures there and dynamical SIT changes connected with the positive AO phase and altered wind stresses which affecting the ice divergence/convergence. The model-based drift sea ice velocity anomalies agree well with the satellite-derived velocity anomalies especially over the Eastern part of the Arctic Ocean displayed in Figure 11. Over the Beaufort Sea and the Western part of the Arctic Ocean the strength of sea ice drift in the RASM simulations is underestimated and the direction differs a bit compared to the satellite data.

345

3.2.4 Internal variability

Previous work by *Ding et al. (2019)* and *Nie et al. (2019)* emphasized the importance of internally generated climate variations for the shift of the AO phases. Here, we examine related regional sea ice variations in the Pan-Arctic and in the BS domains (Figure 12) under the remote AO impact in ensemble forecasts. The Pan-Arctic domain covers the whole Arctic Ocean with

350   borders at the Bering Street (BSr), the Fram Strait (FS), the Barents Sea Opening (BSO) and the Davies Strait (DS). Figure 13 displays the temporal evolution of the mean absolute difference (relative to the ensemble mean) in simulated Pan-Arctic and BS sea ice volume for the RASM 30-member ensemble 6-month forecast simulations from November 1, 2019 through April 30, 2020. Each ensemble member is dynamically downscaling a different NCEP CFSv2 global forecast initialized 24-hr apart at 0000 between 1 and 31 October 2019. The differences among the 30 ensemble members for the Pan-Arctic domain are in

355   the range of 1000 km^3 and show significant positive or negative ice volume departures from the ensemble mean volume. Figure 13 clearly indicates the large internally generated variability of the Pan-Arctic and BS sea ice volume changes in the coupled regional system. Differences in sea ice volume vary significantly between the Pan-Arctic and the BS region and can be even of opposite sign, e.g. as visible in ensemble member 2 and 8. The sea ice evolution distinguishes among all 30 ensemble members. e.g. ensemble members 1, 2, 3, 10, 13, 19, 25, and 26 indicate positive sea ice volume differences of different

360   strength during the winter 2020 in the Pan-Arctic domain, whereas e. g. ensemble members 7, 8, 9, 15, 16, 22, and 23 show negative ice volume differences of varying strength. In the BS ensemble member 2, 4, 8, 12, 19, and 30 indicate different ice volume trends in comparison to the Pan-Arctic domain. To quantify the underlying mechanisms for the Arctic ice volume differences and diverging temporal evolution we display the thermodynamic sea ice volume tendencies (TVT) with combined ice growth and ice melt terms for all 30 ensemble members for the Pan-Arctic and the BS domain in Figure 14 from November

365   2019-March 2020. Compared to the hindcast values (yellow bars) the tendencies in the different months varies both for the Pan-Arctic and BS domain. In February and March 2020 the mean sea ice volume tendencies reaches 73 to 58 km^3/day in the Pan-Arctic. The standard deviation remains similar strong from November-February and becomes weaker in March. The TVT in the BS during January and February are in the range of 6 km^3/day and above 4 km^3/day during March. Standard deviations in the BS are highest in December 2019. In addition, we show the dynamical ice volume tendencies (DVT) in the BS (note

370   that the Pan-Arctic DVTs are zero by definition), which are weaker and indicate a sea ice decline in most ensemble members and all months. Only 6 ensemble members show positive DVT during January and February, but 8 members in March. The hindcast simulation indicates BS dynamical tendencies near-zero in January, negative in February but positive in March 2020. Figures S3, S4 and S5 show the statistical properties, based on differences of daily values, of TVTs for the Pan-Arctic and the BS domains and DVTs for the BS region from November 2019-March 2020. These figures clearly indicate the strong

375   deviations due to internally generated variability in Arctic sea ice growth and dynamical ice deformations. Ensemble members 2 / 8 has been selected as the representation of maximum / minimum ice volume difference for the Pan-Arctic domain. However, those two ensemble members are not representative of the BS, which is why respective ensemble members 4 and 9 are selected. In the RASM hindcast, the Pan-Arctic TVT increases due to ice growth from November until January. The differences between the hindcast and the four selected forecast simulations 2, 4, 8, and 9 are large through all months from

380   November until February and can reach ~20 km^3/day, or ~600 km^3/month. The TVT in BS for the same four ensemble members 2, 4, 8, and 9 is in the range of 3 km^3/day or ~90 km^3/month.

Figures S6 displays the SLP anomalies in November 2019 and January 2020 for the hindcast simulation and the Pan-Arctic ensemble member 2 (positive sea ice anomaly in Figure 13) and Pan-Arctic ensemble member 8 (negative sea ice anomaly in Figure 13). The pressure pattern for ensemble member 8 shows a strong low pressure anomaly in January over Siberia and that

385   for ensemble member 2 a high pressure anomaly in January over the Arctic Ocean. The 500 hPa geopotential heights for the RASM hindcast and the two ensemble members (not shown) indicate a pronounced barotropic structure in the troposphere and emphasize the diverging development of the pressure, temperature and geopotential patterns and the important role of

internally generated variability in sea ice formations as pointed out by *Ding et al. (2019)*. Ocean and sea ice time scales provide memory effects for seasonal sea ice forecasts, but the large atmospheric variability connects sea ice predictability to 390 atmospheric wind predictions of up to 10 days as discussed by *Inoue (2020)* and set inherent limits for seasonal sea ice predictions as pointed out by *Serreze and Stroeve (2015).*

Figure 15 displays the differences of TVTs and DVTs per model grid cell representing the sea ice redistribution between RASM Pan-Arctic ensemble member 2 (positive ice difference in Figure 13) and Pan-Arctic member 8 (negative ice difference in Figure 13). The largest sea ice volume increase occurs in both ensemble members in the BKS and at the north-west side of 395 Greenland. In both ensemble members the thermodynamic ice growth is in the range between 0.5 and 1 m/winter with more enhanced ice growth in the Laptev Seas (not shown). The difference plot indicates differences between the two forecast ensemble members of up to -0.5 m in the BKS and up to 0.3 m over the Arctic Ocean. The accumulated winter (JFM) ice volume tendencies following dynamical and thermo-dynamical drivers are largest in the BS. Bigger ice volume differences occur north-west of Greenland with more than 0.5 m during the winter. The pan-Arctic sea ice volume represents the coupled 400 system response to large-scale forcing and it is a better diagnostic of different sea ice regimes among ensemble members since the sea ice extent and sea ice area is relatively similar in winter. Compared to the dynamical contributions, the thermodynamic growth processes both presented in Fig. 15 lead to greatest differences between the two ensemble members in the BKS and at the ice edge region around Spitsbergen and Greenland.

3.2.5 Case study of positive and negative AO winters

405 To contrast the sea ice conditions and the integrated regional processes and feedbacks for positive and negative winters AO we compare the RASM hindcast results during the MOSAiC winter 2020, with an exceptionallly positive AO phase, against the exceptionally negative AO winter of 2009/2010. Figure S7 displays the AO time series of the AO index from October 2009 until May 2010, which indicates a weakly positive AO phase in November 2009 and the strongest negative AO phase in winter 2010 during the last 60 years (*L'Heureux et al. 2010*). As discussed, e. g. by *Zhao et al. (2019)* the AO phase is closely related 410 to sea ice variability over the Arctic Ocean. Surface heat fluxes in the coupled Arctic climate system in winter are influenced by different positive and negative feedbacks as e. g. vertical ocean convection, atmospheric turbulence, latent heat and cloud formations, long wave radiation, oceanic currents, Arctic storms and atmospheric circulations and can be considered as an integrated quantity related to all these processes. This regional approach has obvious limits, since e. g. *Gong et al. (2020)* showed the existence of a hemispheric planetary wave train propagating from the subtropics through mid-latitudes into the 415 Arctic and back, thereby recharged and amplified over the Arctic through anomalous latent heating over the Greenland Seas and BKS. Figure S8 shows the RASM simulations of SLP and 2m temperature for January 2010, which represents the negative AO phase, given the atmospheric nudging in RASM above 500 hPa. The nudging of the regional coupled Arctic climate system model RASM to the different AO phases allows a rough and quick diagnosis of differences between the surface heat fluxes for the two AO phases.

420 Figure 16 presents the SIT differences and TVT differences between the mean JFM period 2010 and JFM 2020 and the turbulent surface heat fluxes for JFM 2010 and 2020 from the RASM hindcast simulations. During the negative AO winter 2010 SIT was enhanced in the Beaufort- and the Siberian Seas and in a belt from the north coast of Greenland to the Canadian Arctic with SIT differences greater than 1 m. In the western part of Arctic Ocean and the BKS ice thickness was weaker in JFM 2010 compared to JFM 2020. The TVTs indicate stronger sea ice growth over most parts of the Arctic Ocean in JFM 425 2010 except north of Greenland and in parts of the BKS.

During winter under polar night conditions the main component of the surface heat budget is through sensible and latent heat fluxes and a stronger heat release from the ocean to the atmosphere connected to the North Atlantic oceans current occur. Figure 16 displays the surface heat fluxes for JFM 2010 and JFM 2020 and indicates stronger heat fluxes for the positive AO winter phase 2020 in the North Atlantic Ocean south and east of Greenland, in the western BS region and at the North- 430 American coast on the Pacific side. Negative values mean that the ocean is losing heat the atmosphere. The difference plot in

the lower row of Figure 16 identifies enhanced heat flux changes in the North Atlantic around and south of Greenland, along the eastern coast of Greenland and in the western BS with values of 150 W/m^2 during the positive AO phase. Along the Norwegian coast and the eastern BS the turbulent heat fluxes are reduced. On the Pacific side a similar dipole pattern with enhanced fluxes along the North-American coast and reduced fluxes in the Okhots Sea is visible. This difference structure on

435 the North Atlantic side agrees very well with the NCEP based surface heat flux analysis of *Zhao et al. (2019)*, who showed the high correlation between the sensible heat fluxes in this North Atlantic region with the AO index (their Figure 8a). Positive surface heat fluxes in this region are positively correlated with a higher AO phase. The main factor mediating the turbulent surface heat fluxes is the meridional wind component in the Nordic Seas. *Zhao et al. (2019)* showed, that during a positive AO index the atmospheric circulation enhances the transport of warm air and humid into the Arctic along the Norwegian coast

440 through southerly winds and the transport of cold and dry air to the Atlantic along the Greenland coast via northerly winds (see their Figure 10). Figure 16 supports the view of *Gong et al. (2020)* (their Figure 7f) about heating anomalies in the Greenland, BS and Kara Sea as a possible source of planetary wave activity over the Arctic Ocean.

4 Summary and Conclusions

Monthly gridded sea-ice thickness information from remote sensing data based on the ESA CryoSat-2/SMOS Level-4 sea ice
445 thickness data set, produced and disseminated by the Alfred Wegener Institute, Helmholtz Centre for Polar and Marine Research has allowed the determination of Arctic-wide sea ice thickness distributions between the 15 October 2019 and 15 April 2020. We analyzed and compared the satellite sea ice thickness measurements with results from the hindcast simulation using the fully coupled RASM for the time period November 2019 until March 2020. The synthesis of sea ice thickness distribution and ice growth simulated by RASM with the CryoSat-2/SMOS data allows a better understanding of the local and
450 regional coupled atmosphere-ocean-sea ice processes during the period with a positive AO determined from ERA5. A comparison of the SIT for November 2019 and JFM 2020 indicated thicker ice in the central Arctic in the CryoSat2/SMOS data compared to the RASM. In the BS, the Laptev Seas and the Bering Strait the RASM simulations indicates thicker sea ice in the range of up to 1 m compared to the satellite data, partly connected to the impact of surface roughness on the radar freeboards and the retrieval algorithms as discussed by *Landy et al. (2020)*. The agreement between CryoSat-2/SMOS data
455 and the RASM hindcast simulations is favorable with high correlations between 0.74 and 0.76 and a low bias.
Connected to anomalous atmospheric circulation in winter 2019/20, with a positive AO phase from January-March 2020, thickness anomalies of up to 1.3 m occurred in the BS, along the north-eastern Canadian Coast and in the central Arctic Ocean. In-situ sea ice thickness measurements on board the resupply icebreaker „Kapitan Dranitzyn" and thickness measured at the MOSAiC floe were in reasonable agreement with the RASM sea ice thickness simulations considering an obvious bias of 0.4
460 m between the ship- and ground-based measurements at the MOSAiC floe. In January 2020 strong ice growth takes place in the BKS and the Siberian Seas and the Bering Strait. In February the strongest ice growth anomalies occur over the Beaufort Sea and in March over the mid-Arctic Ocean and parts of the BS and at the east coast of Greenland. In February and March 2020 weaker sea ice growth is visible in the Laptev Sea, east of Greenland and the Davis Strait. The positive sea ice thickness anomaly in the BS during winter 2020 is a result of enhanced ice growth connected with the colder temperature anomalies in
465 this area, and a consequence of intensified sea ice convergence and ice shears. Compared to the dynamic contributions the thermodynamic growth processes lead to greatest differences in the BKS and at the ice edge region around Spitsbergen and Greenland. In January and February 2020 a stronger contribution to the ice growth originated from sea ice deformations driven by atmospheric wind forcing. The model-simulated ice divergence and ice shear have positive values in different regions of the BKS. There is negative ice divergence (representing convergence) in the region of greatest sea ice growth, whereas the ice
470 shear processes following wind stresses indicates here positive values.

From January until March 2020 low-pressure anomalies developed over the Eastern Arctic induced northerly winds from the cold Arctic Ocean to the BS and accelerating the southward drift of the MOSAiC ice floe in the Transpolar Drift. During March the low-pressure anomalies were located north of the Laptev Sea, inducing westerly wind anomalies following Arctic cyclone tracks in the BKS and keeping the cold air in the Arctic. The model-simulated and satellite-derived sea ice velocity anomalies during January-March 2020 indicates a strong acceleration of the Transpolar Drift during the MOSAiC winter with intensified speeds up to 6 km/day. In the RASM hindcast, the Pan-Arctic TVT increases due to ice growth from November until January. The unusual shift to a positive AO phase in the MOSAiC winter 2019/20 could contain a strong portion of internally-generated climate variability in sea ice formation in agreement with *Ding et al. (2019).* To quantify the underlying mechanisms for the Arctic ice volume differences and diverging temporal evolution we display the thermodynamic sea ice volume tendencies with combined ice growth and ice melt terms for all 30 ensemble members in the forecast mode for the Pan-Arctic and the BS domain from November 2019-March 2020. In February and March 2020 the mean sea ice volume tendencies reaches 110 km^3/day in the Pan-Arctic and strong deviations occur due to internally generated variability in Arctic sea ice growth and dynamical ice deformations. The differences between the hindcast and the four selected forecast simulations 2, 4, 8 and 9 are largest in November and December and can reach ~20 km^3/day, or ~600 km^3/month. For selected members of the model ensemble the dynamical contributions due to wind advection and thermo-dynamic growth processes have been computed, which show the largest differences in the BS region. The accumulated winter ice volume tendencies following dynamic and thermodynamic drivers are largest in the BS and linked to surface turbulent heat and momentum fluxes and oceanic convergence.

During the negative AO winter 2010, sea ice growth was enhanced in the Beaufort- and the Siberian Seas and in a belt from the north coast of Greenland to the Canadian Arctic with sea ice differences greater than 1 m compared to the positive AO winter 2020. The surface heat fluxes for JFM 2010 and JFM 2020 indicates much stronger heat fluxes for the positive AO winter phase 2020 in the North Atlantic Ocean south of Greenland, whereas in the BS region and on the Pacific side the patterns look similar. This result supports the idea of *Sato et al. (2014),* that sea ice changes in the BS are under the control of atmospheric circulation over the Norwegian Seas and an enhanced southerly wind advection connected to the northward shift of the Gulf stream, which influences the temperature and sea ice extent in the BS via a northward shifted North Atlantic storm track, which needs more in-depth investigation.

Acknowledgement

This work was carried out as part of the Multidisciplinary drifting Observatory for the Study of Arctic Climate (MOSAiC) funded by the German Ministry for Education and Research (BMBF) under grant N-2014-H-060_Dethloff.

The production of the merged CryoSat-SMOS sea ice thickness data v2.02 was funded by the ESA project SMOS & CryoSat-2 Sea Ice Data Product Processing and Dissemination Service, and data from November 2010 to April 2020 were obtained from AWI (ftp://ftp.awi.de/sea_ice/product/cryosat2_smos/v202/). The ERA5 data were provided by the European Centre for Medium-Range-Weather Forecasts (ECMWF) in Reading.

Sea ice thickness data used in this manuscript was produced as part of the international Multidisciplinary drifting Observatory for the Study of the Arctic Climate (MOSAiC) with the tag MOSAiC20192020 and Project ID AWI_PS122.

WM, YL, JC and JCK acknowledge partial support of the RASM contribution from the following programs: the U.S. Department of Energy (DOE) Regional and Global Model Analysis (RGMA), the Office of Naval Research (ONR) Arctic and Global Prediction (AGP) and National Science Foundation (NSF) Arctic System Science (ARCSS), and RO from the Ministry of Science and Higher Education in Poland. The U.S. Department of Defense (DOD) High Performance Computer Modernization Program (HPCMP) provided computer resources for RASM simulations analyzed here.

KD, DH and AR acknowledge the funding by the Deutsche Forschungsgemeinschaft (DFG, German Research Foundation) – project number 268020496 – TRR 172, within the Transregional Collaborative Research Center "ArctiC Amplification: Climate Relevant Atmospheric and SurfaCe Processes, and Feedback Mechanisms (AC)[3]".

TK, DH and AR acknowledge the project "Quantifying Rapid Climate Change in the Arctic: regional feedbacks and large-scale impacts (QUARCCS)" funded by the German and Russian Ministries of Research and Education.

515

Competing interests

The authors declare no competing interests.

520 **Author contributions**

K. D. and W. M. conceived the study and wrote the paper. S. H., Y. L., H. F. G., T. K., C. H., D. H., and R. R. undertook the data analysis and developed the methods. V. B., J. J. C., J. C. K., R. O., M. R., A. R., J. S., and A. S. contributed to the interpretation of results. All authors commented on the manuscript.

525

530

535

540

545

550

References

555   AARI Russian North Polar Drifting Station Data from NSIDC, 193, Res. Data Archive at NCAR, https://doi.org/10.5065/V47S-KW40

Armitage, T. W. K., et al. 2018, Arctic sea level and surface circulation response to the Arctic Oscillation. Geophys. Res. Lett., 45, 6576–6584, doi:10.1029/2018GL078386

Barton, I., et al., 2018, Observed Atlantification of the Barents Sea causes the polar front to limit the expansion of winter Ssa

560   ice, J. Phys. Oceanography, 1849-1866, DOI: https://doi.org/10.1175/JPO-D-18-0003.1

Belter, H. J., et al. , 2020, Interannual variability in Transpolar Drift ice thickness and potential impact of Atlantification, The Cryosphere Discuss., https://doi.org/10.5194/tc-2020-305, in review.

Blackport, R., et al., 2019, Minimal influence of reduced Arctic sea ice on coincident cold winters in mid-latitudes. Nat. Clim. Chang. 9, 697–704, https://doi.org/10.1038/s41558-019-0551-4

565   Bushuk, M., et al., 2019, The value of sustained Ocean observations for sea ice predictions in the Barents Sea, J. Climate, 32, 7017-7035.

Cassano, J. J., et al., 2017, Development of the Regional Arctic System Model (RASM): Near-Surface Atmospheric Climate Sensitivity, J. Climate, 30, 5729-5753.

Cohen, J., et al., 2012, Arctic warming, increasing snow cover and widespread boreal winter cooling, Env. Res. Lett., 7,

570   014007.

Cohen, J., et al., 2014. Recent Arctic amplification and extreme mid-latitude weather. Nat. Geosci. 7, http://dx.doi.org/10.1038/ngeo2234.

Dethloff, K., et al., 2006, A dynamical link between the Arctic and the global climate system. Geophys. Res. Lett., 33, L03703, doi: 10.1029/2005GL025245.

575   Ding, Q., et al, 2019: Fingerprints of internal drivers of Arctic sea ice loss in observations and model simulations. Nat. Geosci., 12, 28–33, https://doi.org/10.1038/s41561-018-0256-8.

Dorn, W., et al., 2007, Sensitivities and uncertainties in a coupled regional atmosphere-ocean-ice model with respect to the simulation of Arctic sea ice, J. Geophys. Res., 112, D10118, doi:10.1029/2006JD007814.

Dorn, W., et al, 2009, Improved simulation of feedbacks between atmosphere and sea ice over the Arctic Ocean in a coupled

580   regional climate model, Ocean Model., 29, 103–114, doi:10.1016/j.ocemod.2009.03.010, 2009.

Frolov, I. E., et al., 2005, The Arctic Basin: Results from the Russian Drifting Stations. Praxis Publishing. Chichester, 270 pp.

Gammelsrød, T., et al., 2009, Mass and heat transports in the NE Barents Sea: Observations and models, Journal of Marine Systems, 75, 56-69, ISSN 0924-7963, https://doi.org/10.1016/j.jmarsys.2008.07.010.

Gong, T. et al., 2020, Rossby Wave Propagation from the Arctic into the Midlatitudes: Does It Arise from In Situ Latent

585   Heating or a Trans-Arctic Wave Train? J. Climate, 33, 3619-3633.

Hendricks, S. and Ricker, R., 2019, Product User Guide & Algorithm Specification: AWI CryoSat-2 Sea Ice Thickness (version 2.2), Technical Report, https://epic.awi.de/id/eprint/50033/

Haas, C., 1998, Evaluation of ship-based electromagnetic-inductive thickness measurements of summer sea-ice in the Bellingshausen and Amundsen Seas, Antarctica, Cold Regions Science and Technology,27,1-16.

590   Haas, C., et val., 1999, Comparison of a long track EM ice thickness profiles with ship performance data, POAC '99: Proc 15th Int Conf on Port and Ocean Engineering Under Arctic Conditions, Espoo, Finland, 1999, J Tuhkuri, K Riska, eds, Helsinki Univ Techn, Ship Lab,1, 343-353.

Hersbach, H. and D. Dee, 20016, ERA5 reanalysis is in production, ECMWF Newsletter 147, https://www.ecmwf.int/en/newsletter/147/news/era5-reanalysis-production.

595   Inoue, J., et al., 2012, The role of Barents Sea ice in the wintertime cyclone track and emergence of a warm-Arctic cold-Siberian anomaly. J. Climate 25, 2561e2568. http://dx.doi.org/10.1175/JCLI-D-11-00449.1.

Inoue, J., 2020, Review of forecast skills for weather and sea ice in supporting Arctic navigation, Polar Sci., in press, https://doi.org/10.1016/j.polar.2020.100523.

Jaiser, R., et al., 2012, Impact of sea ice cover changes on the Northern Hemisphere atmospheric winter circulation, Tellus, 600 64, doi:10.3402/tellusa.v64i0.11595.

Johannessen O. M. et al., 2004, Arctic climate change: Observed and modelled temperature and sea ice variability. Tellus A 56, 328–341.

Kim, B.-M., et al., 2014, Weakening of the stratospheric polar vortex by Arctic sea-ice loss. Nat. Commun. 5, https://doi.org/10.1038/ncomms5646.

Kolstad, E. W. and J. A. Screen, 2019, Nonstationary relationship between autumn Arctic sea ice and the winter North Atlantic Oscillation, Geophys. Res. Lett., 46, 7583-7591.

Krumpen, T., et al., 2020, The MOSAiC ice floe: sediment-laden survivor from the Siberian shelf, The Cryosphere, https://doi.org/10.5194/tc-2020-64

Kwok, R., et al., 2013, Arctic sea ice circulation and drift speed: Decadal trends and ocean currents. J. Geophys. Res. Oceans, 610 118, 2408–2425. https://doi.org/10.1002/jgrc.20191

Landy, J. C., et al., 2020, Sea ice roughness overlooked as a key source of uncertainty in CryoSat-2 ice freeboard retrievals. J. Geophys. Res. Oceans, 125, e2019JC015820. https://doi.org/10.1029/2019JC015820

Large, W. G., & Yeager, S. G., 2008, The global climatology of an interannually varying air–sea flux data set. Climate Dynamics, 33, 341-364. doi:10.1007/s00382-008-0441-3

Lawrence, Z. D., et al., 2020, The remarkably strong Arctic stratospheric polar vortex of winter 2020: Links to record-breaking Arctic Oscillation and ozone loss. J. Geophys. Res., DOI: 10.1002/essoar.10503356.1

L'Heureux M. et al., 2010, Unusual extremes in the negative phase of the Arctic Oscillation during 2009, Geo. Res. Lett. 37, L10704, doi:10.1029/2010GL043338

Liptak, J. and C. Strong, 2014, The winter atmospheric response to sea ice anomalies in the Barents Sea, J. Climate, 27, 914-620 924

Long, Z. and W. Perrie, 2017, Changes in Ocean Temperature in the Barents Sea in the Twenty-First Century, J. Climate, 30,5901-5921, DOI: https://doi.org/10.1175/JCLI-D-16-0415.1

Maslowski, W. et al., 2012, The Future of Arctic Sea Ice. Ann. Rev. Earth Plant. Sci. 40: 625-654.

McCusker, K. E. et al., 2016, Twenty-five winters of unexpected Eurasian cooling unlikely due to Arctic sea-ice loss, Nat. 625 Geosci., 9, 838-842, https://doi.org/10.1038/ngeo2820.

Nakamura, T., et al., 2015, A negative phase shift of the winter AO/NAO due to the recent Arctic sea-ice Reduction in late autumn. J. Geophys. Res. 120, 3209-3227. doi:10.1002/2014JD022848.

Neumann, T. , et al., 2019, The ice, cloud and land elevation satellite-2 mission, A global geolocated photon product, Rem. Sensing Environm. 223, https://doi.org/10.1016/j.rse.2019.111325

Nie Y. et al., 2019, Stratospheric initial conditions provide seasonal predictability of the North Atlantic and Arctic Oscillations, 630 Environ. Res. Lett., 17, 034006

Nie, J., et al., 2008, Northern hemisphere storm tracks in strong AO anomaly winters. Atmos. Sci. Lett., 9: 153-159. doi:10.1002/asl.186

Onarheim, I. H., et al. 2015, Skillful prediction of Barents Sea ice cover, Geophys. Res. Lett., 42, 5364-5371.

635 Orsolini Y. et al., 2013 Impact of snow initialization on sub-seasonal forecasts, Clim. Dynnamics., 41, 1969–82

Peings Y. and G. Magnusdottir, 2014, Response of the wintertime Northern Hemisphere atmospheric circulation to current and projected Arctic sea ice decline: a numerical study with CAM5, J. Climate, 27, 244–64

Platov, G. et al., 2020, Characteristics of Atmospheric Circulation Associated with Variability of Sea Ice in the Arctic Geosciences, 10, 359; https://doi.org/10.3390/geosciences10090359

640 Polarstern: Alfred-Wegener-Institut Helmholtz-Zentrum für Polar- und Meeresforschung., 2017, Polar Research and Supply Vessel POLARSTERN Operated by the Alfred-Wegener-Institute. Journal of large-scale research facilities, 3, A119. http://dx.doi.org/10.17815/jlsrf-3-163

Polyakov, I. V., et al., 2020. Weakening of Cold Halocline Layer Exposes Sea Ice to Oceanic Heat in the Eastern Arctic Ocean. Journal of Climate, 33, 8107–8123, doi:10.1175/JCLI-D-19-0976.1.

645 Proshutinsky A, and Johnson M. 1997. Two circulation regimes of the wind-driven Arctic Ocean. J. Geophys. Res. 102, 12 493–12 514. (10.1029/97JC00738.

Ricker, R., et al., 2017, A weekly Arctic sea-ice thickness data record from merged CryoSat-2 and SMOS satellite data, The Cryosphere, 11, 1607-1623, https://doi.org/10.5194/tc-11-1607-2017.

Ricker, R., 2019, CryoSat-2/SMOS Merged Product, Description Document (PDD), Technical Report v1.2,
650 https://earth.esa.int/eogateway/catalog/smos-cryosat-l4-sea-ice-thickness

Roberts, A. F., et al., 2018, Quality control for community-based sea-ice model development, Phil. Trans. R. Soc., A376, 2017.0344.

Sato, K. et al., 2014, Influence of the Gulf Stream on the Barents Sea ice retreat and Eurasian coldness during early winter, Environ. Res. Lett. 9, 08400.

655 Schlichtholz, P., 2019, Subsurface ocean flywheel of coupled climate variability in the Barents Sea hotspot of global warming, Nature Sci. Rep., 9, 13692, https://doi.org/10.1038/s41598-019-49965-6.

Screen, J. A., et al., 2013, The Atmospheric Response to Three Decades of Observed Arctic Sea Ice Loss, J. Climate, 26, 1230-1248.

Serreze, M. C, et al., 1997, Icelandic Low Cyclone Activity: Climatological Features, Linkages with the NAO, and
660 Relationships with Recent Changes in the Northern Hemisphere Circulation, J. Climate, 10, 453–464.

Serreze, M. C. and J. Stroeve, 2015, Arctic sea ice trends, variability and implications for seasonal ice forecasting, Phil. Trans. R. Soc., A373:20140159.

Smedsrud, L. H., et al., 2013: The role of the Barents Sea in the Arctic climate system. Rev. Geophys., 51, 415–449, https://doi.org/10.1002/rog.20017.

665 Sokolova, E. et al., 2007, Planetary and synoptic scale adjustment of the Arctic atmosphere to sea ice cover changes, Geophys. Res. Lett., 34, L17816.

Spreen, G., et al., 2008, Sea ice remote sensing using AMSR-E 98 Ghz channels, J. Geophys. Res., 113, C02S03, doi:10.1029/2005JC003384.

Steele, M., et al., 2001. PHC: A Global Ocean Hydrography with a High-Quality Arctic Ocean. J. Climate, 14, 2079-2087.

670 Stern, H. L. and Moritz, R. E., 2002, Sea ice kinematics and surface properties from RADARSAT synthetic aperture radar during the SHEBA drift, J. Geophys. Research (Oceans), 107, no. C10, 2002. doi:10.1029/2000JC000472.

Tian-Kunze, X., et al., 2014, SMOS-derived thin sea ice thickness: algorithm baseline, product specifications and initial verification, The Cryosphere, 8, 997-1018, doi: 10.5194/tc-8-997-2014.

Tilling, R. L., et al., 2018, Estimating Arctic sea ice thickness and volume using CryoSat-2 radar altimeter data, Advances in
675 Space Research, 62, 1203-1225

Trofimov, A., et al., 2020, Meteorological and oceanographic conditions, ICES Scient. Rep., 2, 30-46, WG on the integrated asessments of the Barents Sea, ICES. 2020. Working Group on the Integrated Assessments of the Barents Sea (WGIBAR). ICES Scientific Reports. 2:30. 206 pp, http://doi.org/10.17895/ices.pub.5998

Zhao, J. et al., 2019, Positive and negative feedbacks related to the Arctic Oscillation revealed by air-se heat fluxes, Tellus,
680 71, 1596519.

Zwally, H.J., et al., 2002, ICESat's laser measurements of polar ice, atmosphere, ocean, and land, Journal of Geodynamics 34, 405-445.

		Nov 2019	Dec 2019	Jan 2020	Feb 2020	Mar 2020
CS2-SMOS	Mean (m)	1,14	1,17	1,24	1,41	1,61
	S.D.	0,71	0,66	0,65	0,71	0,77
RASM	Mean (m)	0,96	1,06	1,23	1,45	1,63
	S.D.	0,59	0,56	0,57	0,58	0,61
Corr. Coef		0,74	0,74	0,75	0,76	0,74
Bias		-0,18	-0,1	-0,01	0,04	0,01
RMSD		0,52	0,46	0,43	0,47	0,51

685

Table 1. Comparison of mean sea ice thickness (Mean), standard deviation (S.D.), correlations, bias and root mean square error (RMSD) between CryoSat2/SMOS satellite data and RASM simulations for November 2019 until March 2020.

690
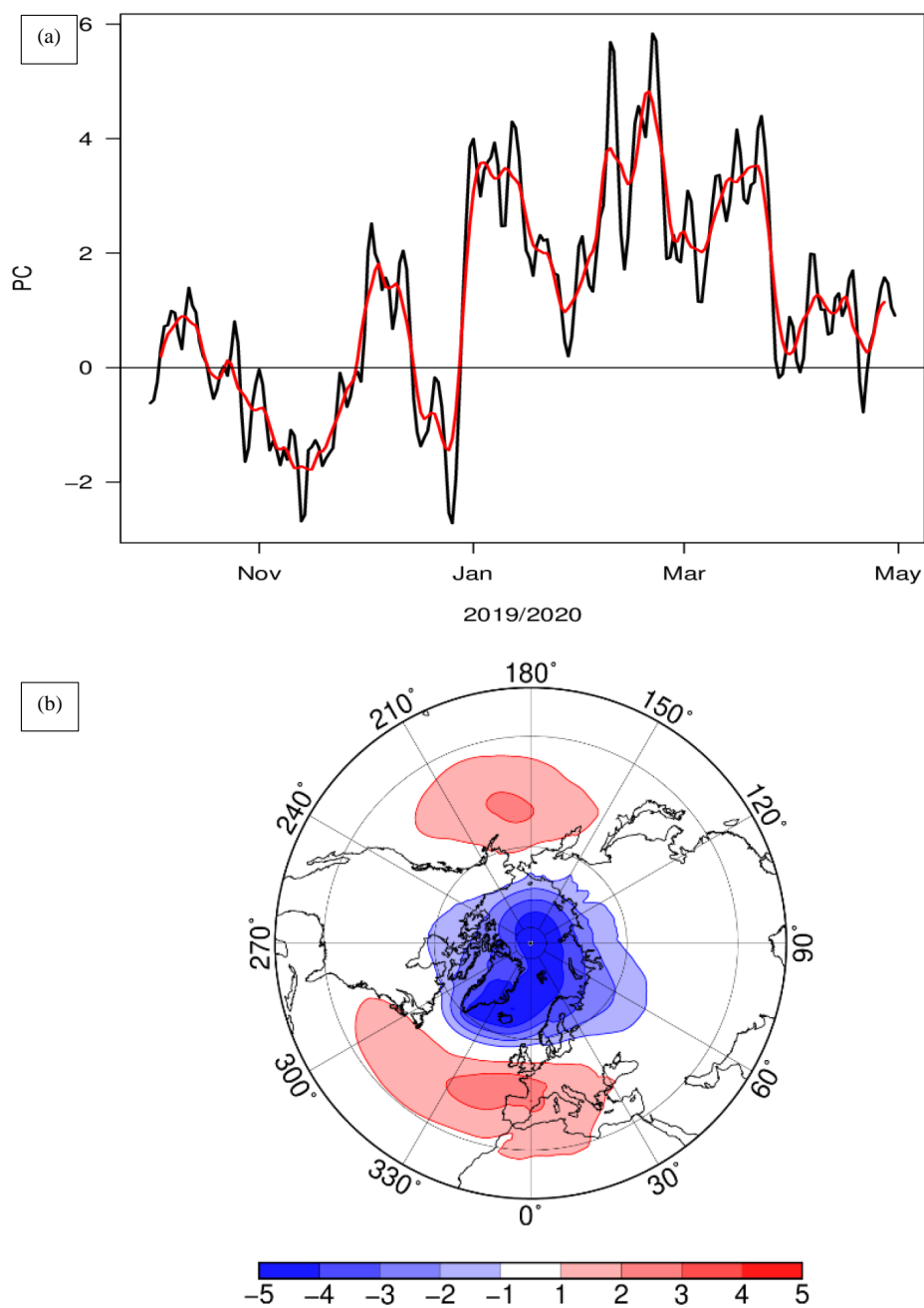
Figure 1: (a) Time series of daily values of the AO index from October 2019 to April 2020 (black line) with 7-day running mean (red line) and (b) the spatial AO pattern from 1979-2000 based on ERA5.
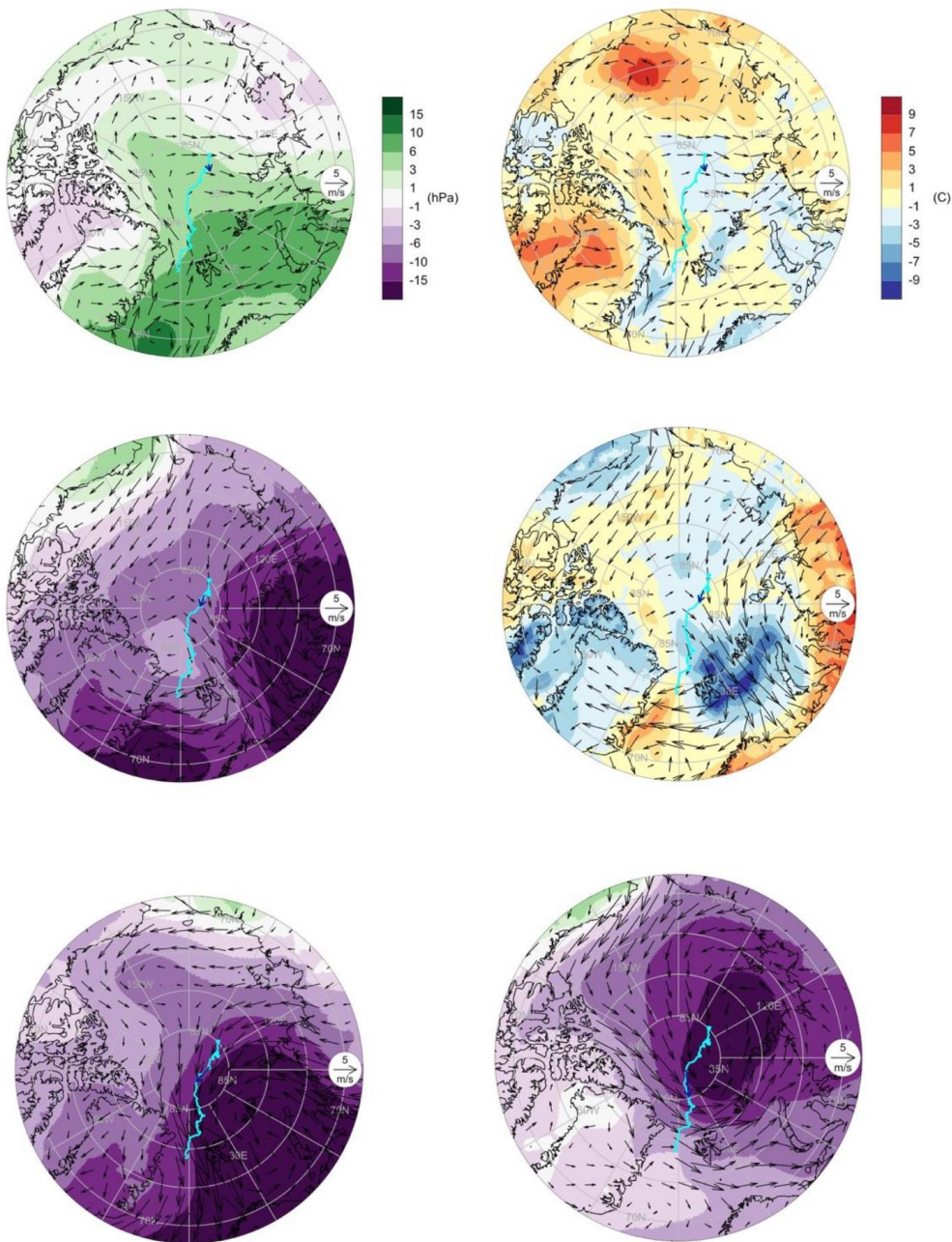
Figure 2. Sea level pressure anomaly (hPa) (left) and 2 m temperature anomaly (K) (right) compared to the climate mean 2010-2019 for November 2019 (top row) and January 2020 (middle row) based on ERA5. Sea level pressure anomalies (hPa) for February (left) and March (right) 2020 (bottom row). Arrows display the direction and strength of 10 m atmospheric winds. The cyan lines indicate the MOSAiC ice floe track from October 2019 until August 2020. Small blue arrows indicate the MOSAiC location and drift of the respective month.
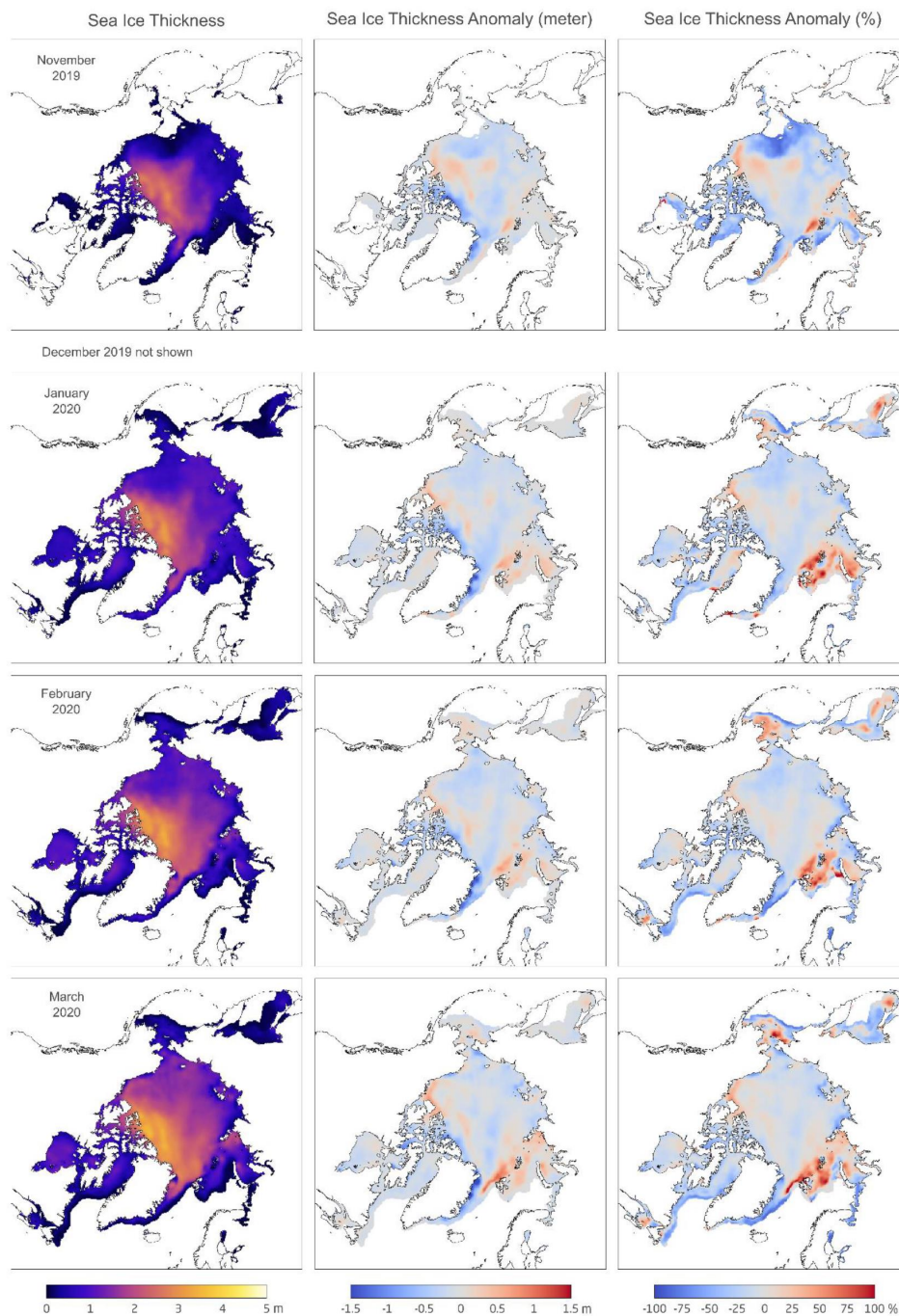
Figure 3. Sea ice thickness (left) and anomaly in meter (middle) and anomaly in percent (right) for November 2019 (top) through March
2020 (bottom) [December 2020 not shown] based on CryoSat-2/SMOS satellite data analysis compared to the mean condition in the entire
705   data record (2010-2019).
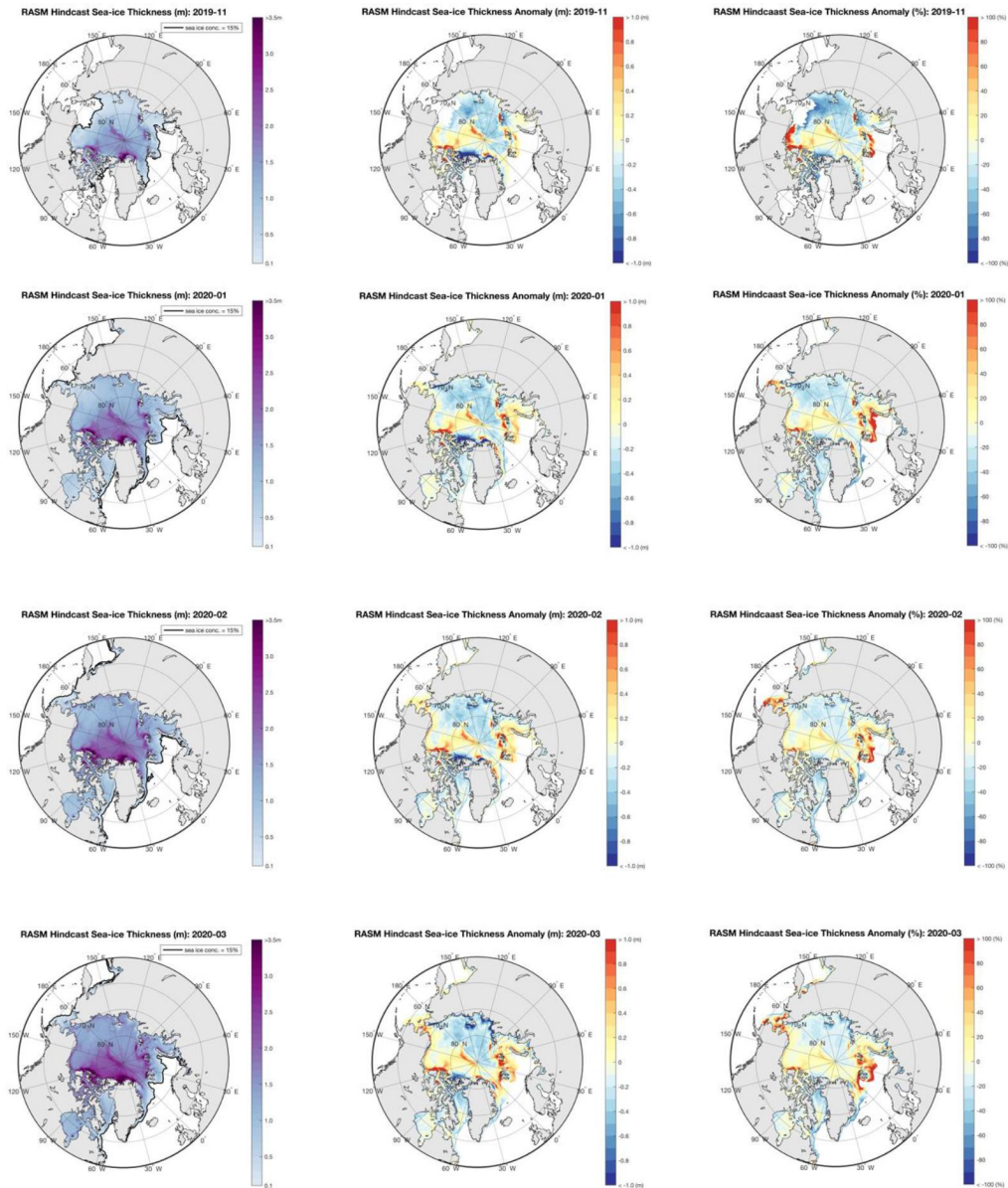
Figure 4. Sea ice thickness (m; black countour line for 15% sea ice concentration; left) and anomalies: in meter (middle), in percent (right) for November 2019 (top), January 2020 (2nd row), February 2020 (3rd row), and March 2020 (bottom) from the RASM hindcast simulation compared to the climate mean 2010-2019.

710
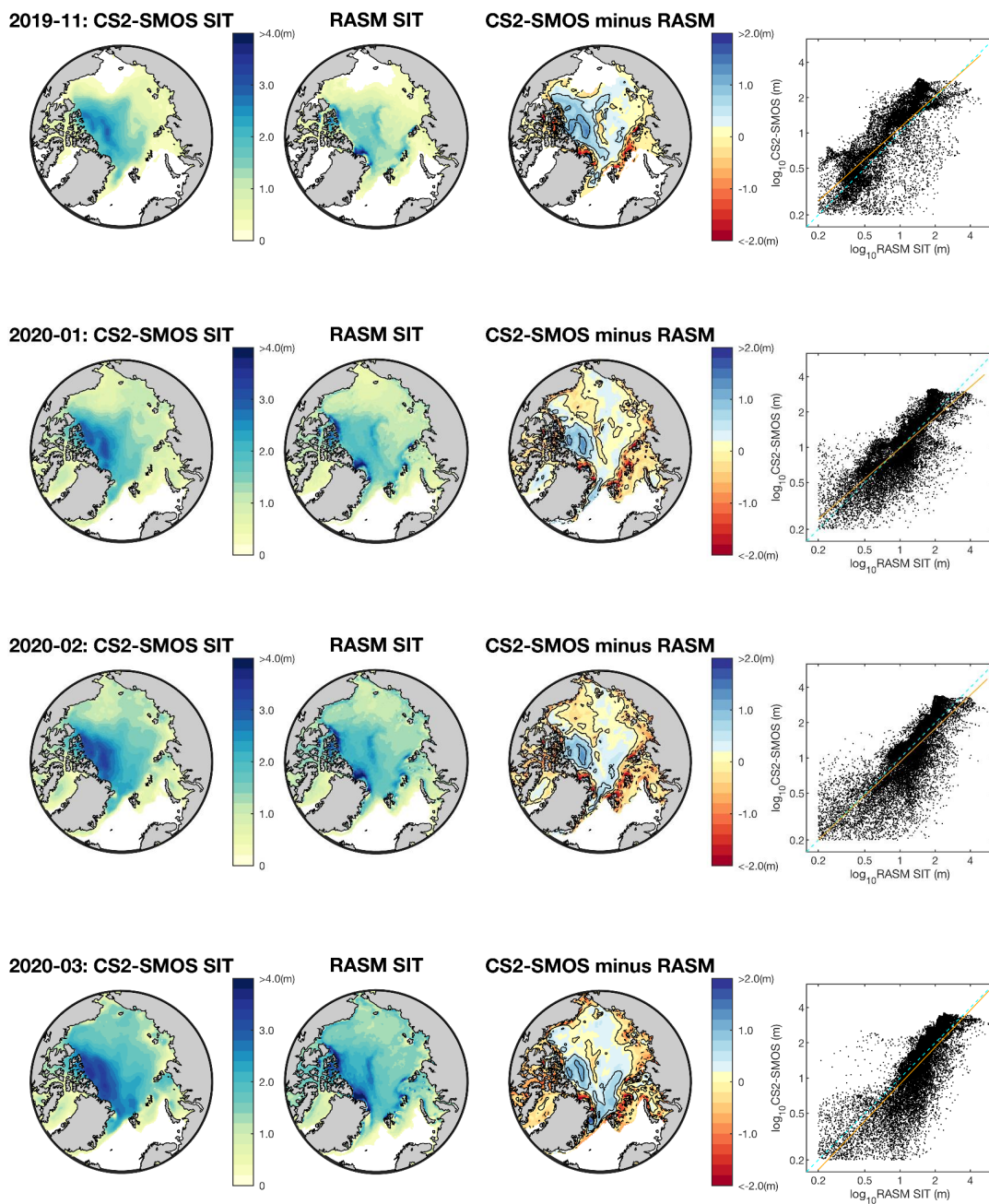
Figure 5. Sea ice thickness (m) for November 2019 (top), January (2nd row) and February 2020 (3rd row) and March 2020 (bottom) based
715 on CryoSat2/SMOS (left column), RASM simulations (2nd column) and the differences "CryoSat2/SMOS minus RASM" (3rd column). The
right column shows the scatter and correlation plots between CryoSat2/SMOS data and RASM results.
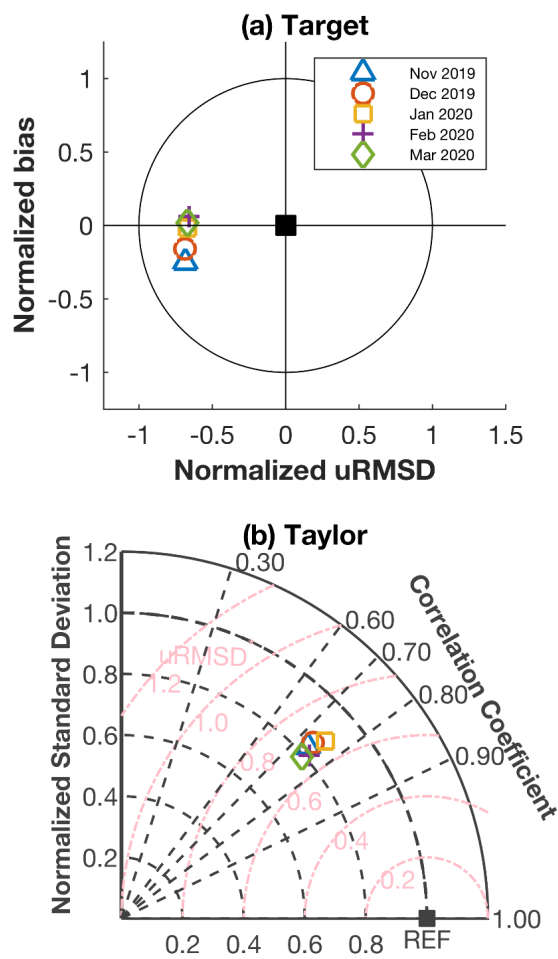
Figure 6. Target diagram (a) of bias and root mean square difference between model sea ice thickness simulations from November 2019-
720   March 2020 and CryoSat2/SMOS and Taylor diagram (b) of standard deviation and correlation between RASM simulations and satellite
data.
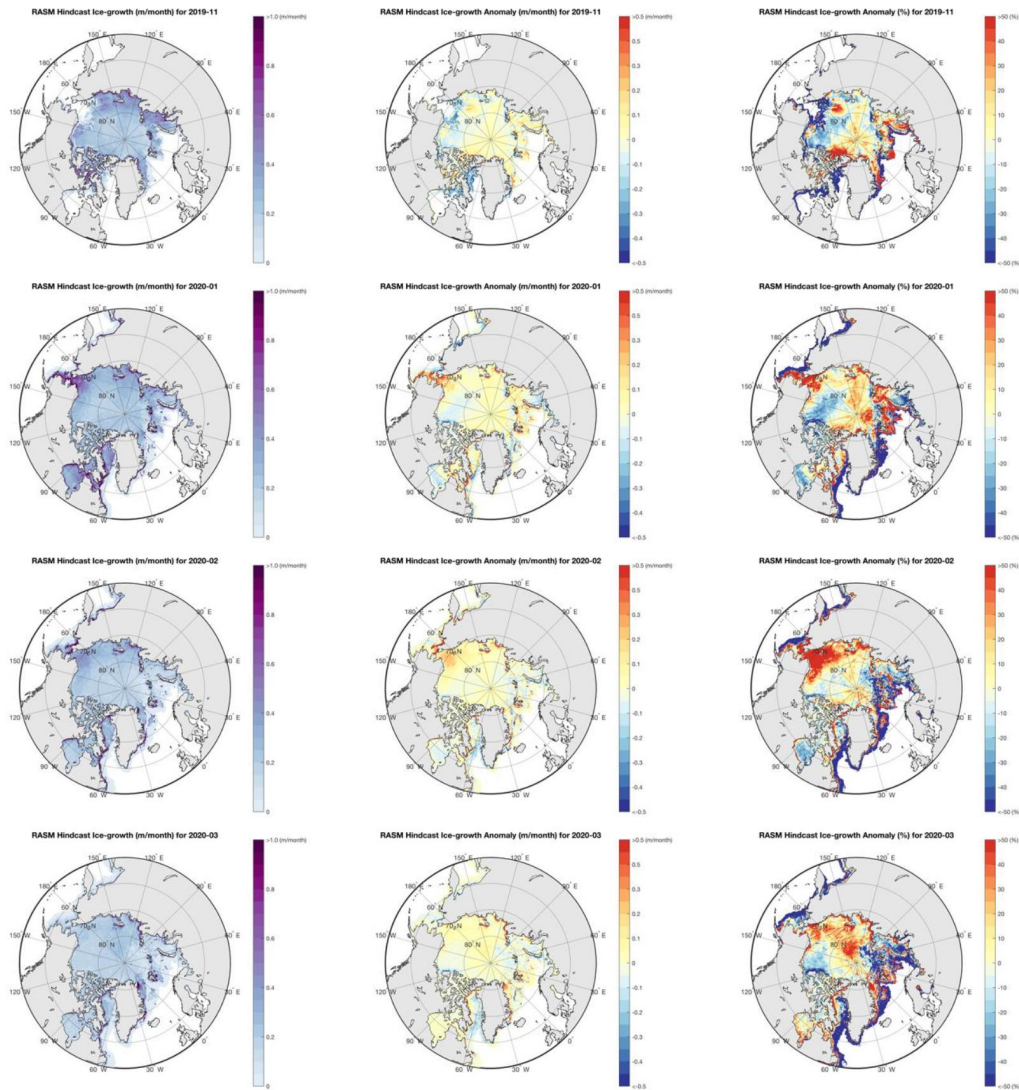
725

Figure 7. The integrated sea ice growth (m/month; left) and sea ice growth anomaly in m/month (middle) and in percent (right) for
November 2019 (top), January 2020 (2nd row), February 2020 (3rd row), and March 2020 (bottom) from the RASM hindcast simulation
compared to the climate mean 2010-2019.

730

735
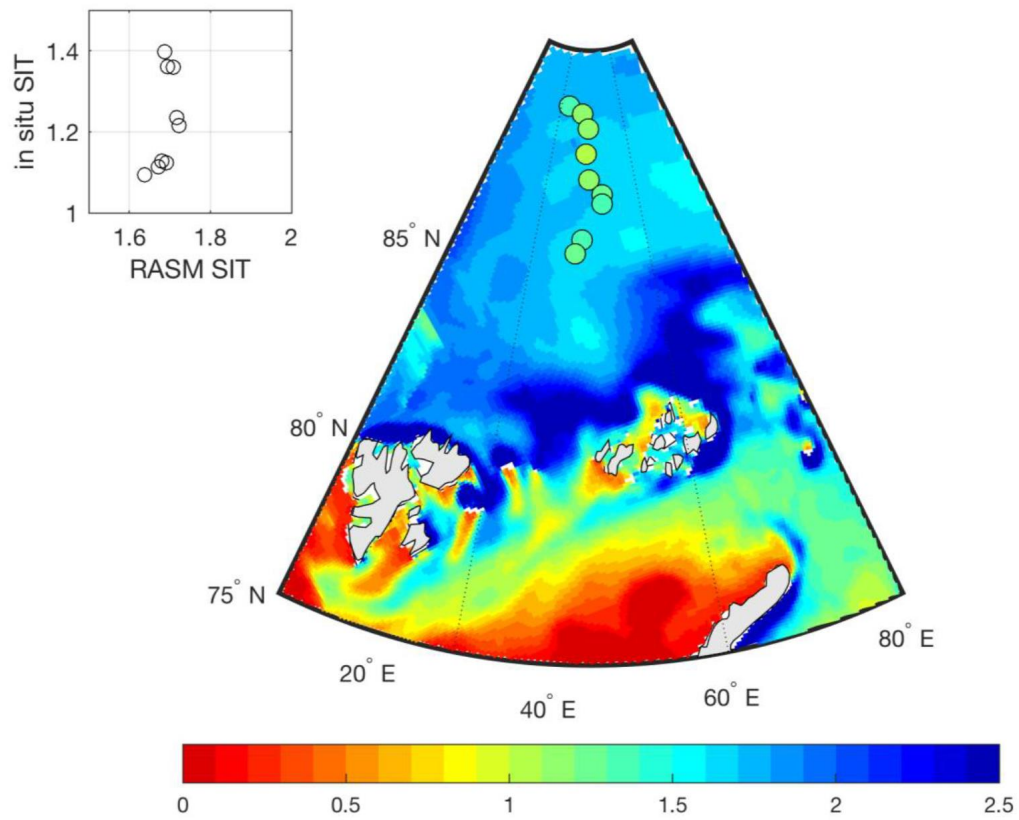
Figure 8. Mean sea ice thickness (m; shading) from the RASM hindcast simulation during March 6-14 and daily EM ice thickness measurements (m; circles) on Kapitan Dranitzyn from 6-14 March 2020. The small black picture (left) compares the in situ sea ice thickness measurements (m) with the corresponding RASM simulations at all points indicated by circles in the coloured plot (right).

740

745

750

755
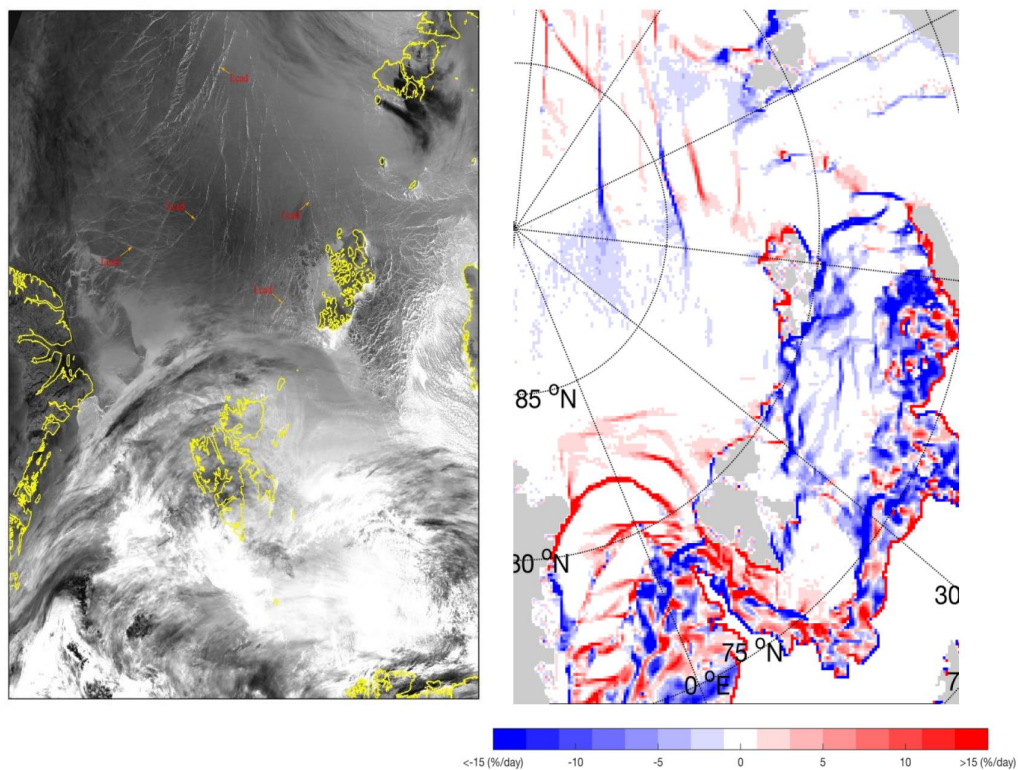
Figure 9. Sea ice lead structures in data from infrared channel 5 of the NOAA-20 satellite with the maximum possible resolution (375 m)
on 5th March 2020 with identification of leads. These data were obtained using the VIIRS instrument (Visible / Infrared Imager Radiometer
Suite), installed on board the NOAA-20 satellite (left). Sea ice divergence (%/day) on 5th March 2020 in the RASM simulation (right).
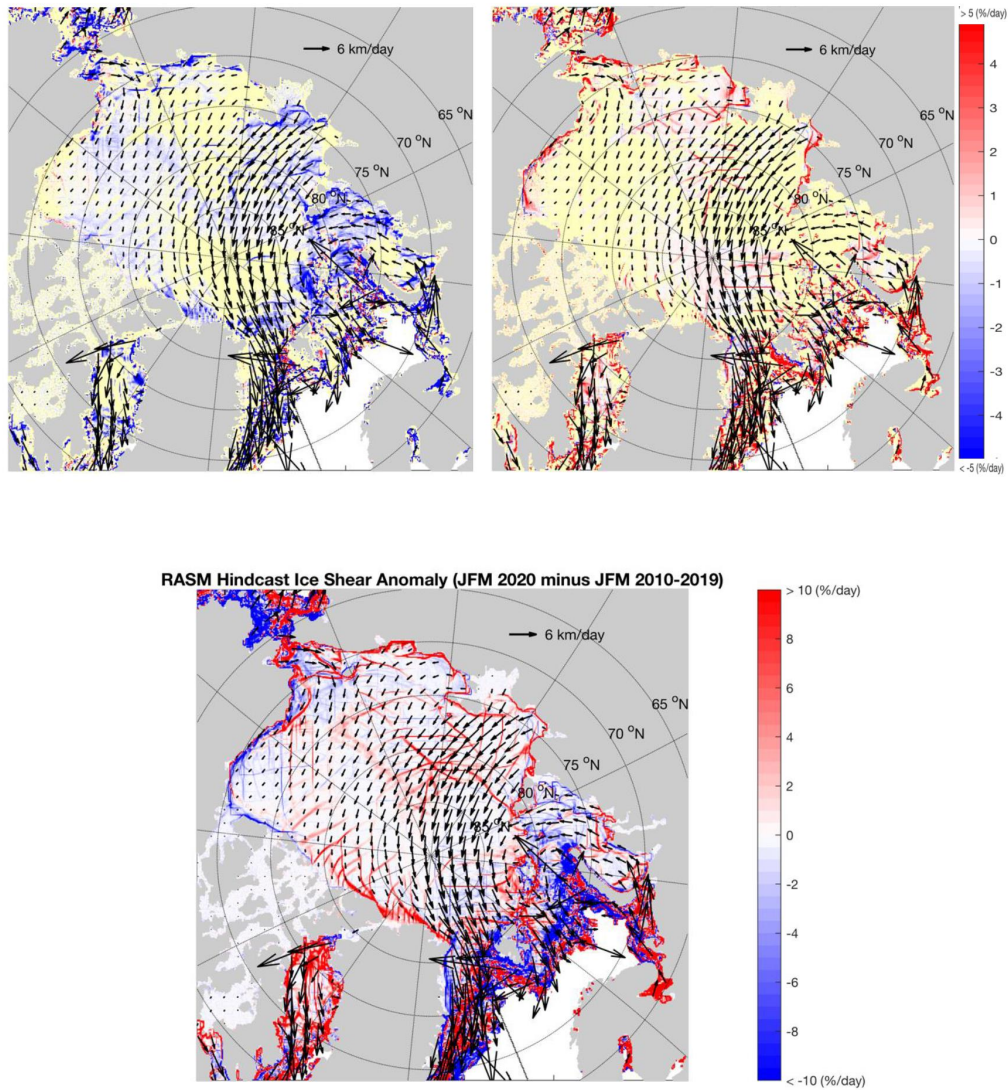
Figure 10. Anomalies of ice convergence (top left; where the blue shading represents more convergence) and divergence (top right; where the red shading represents more divergence). In both graphs yellow shading represents zero values. Bottom graph displays ice shear (%/day) from the RASM hindcast simulation for January-March 2020 compared to the climate mean 2010-2019.
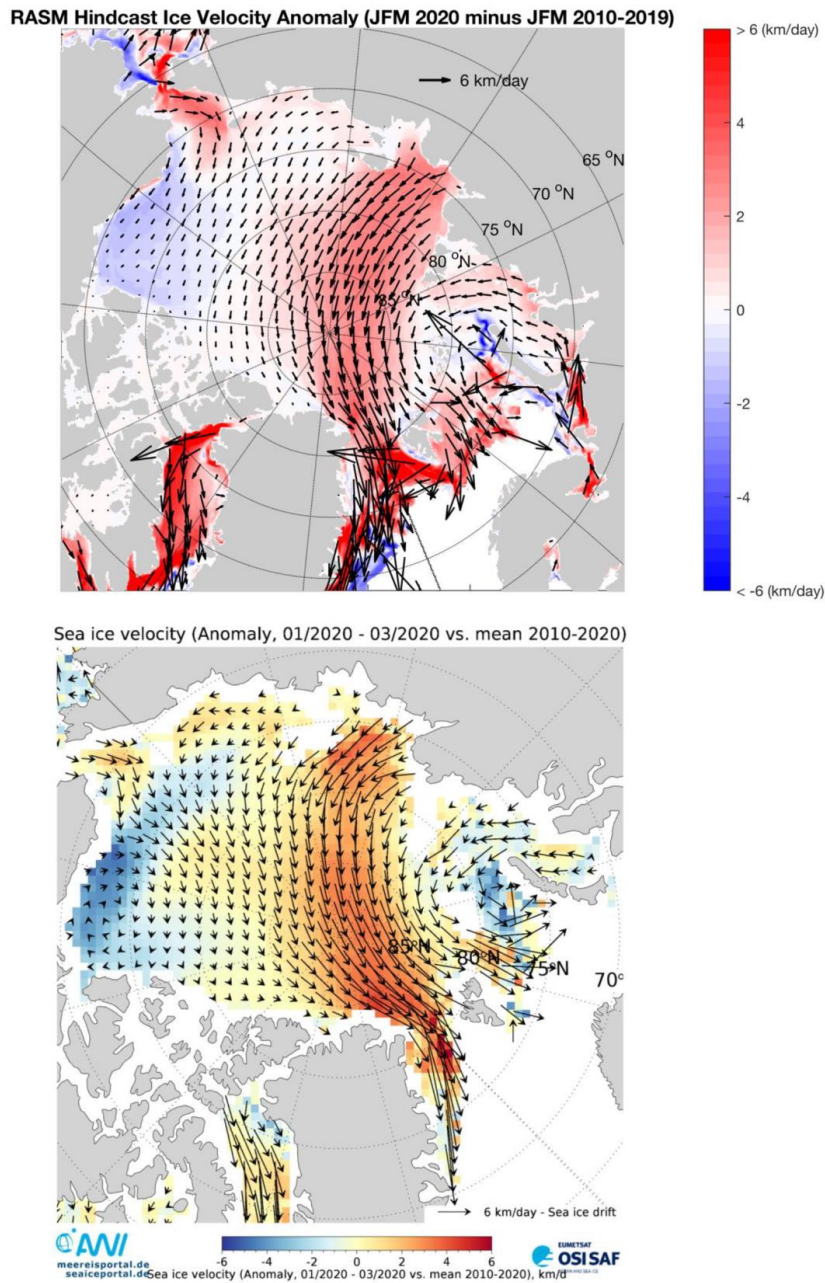
Figure 11. RASM simulations of sea ice velocities (top) and satellite estimated sea ice velocities (km/day) (bottom) for January-March 2020 compared to the climate mean 2010-2019.
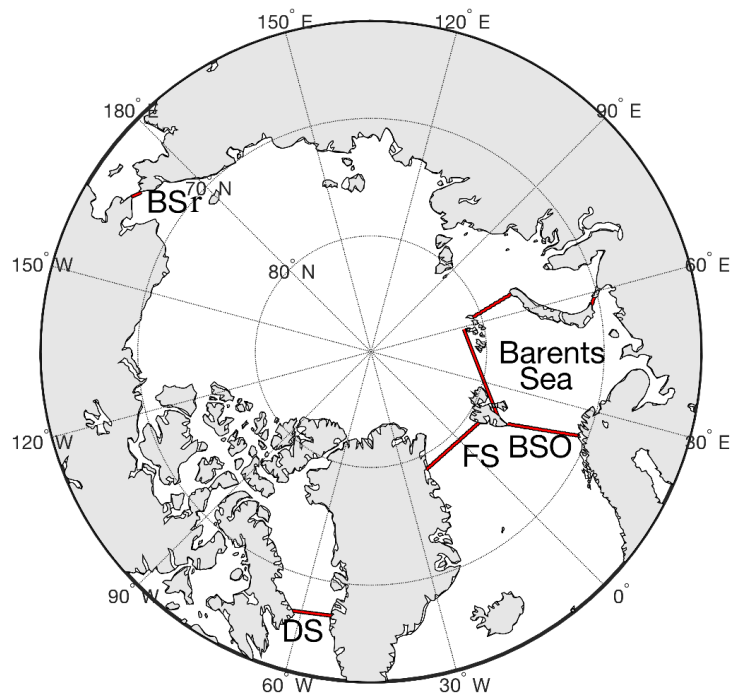
800

Figure 12. The Pan-Arctic and the Barents Sea integration domains used for the computation of the sea ice volume tendencies in Figure 13.
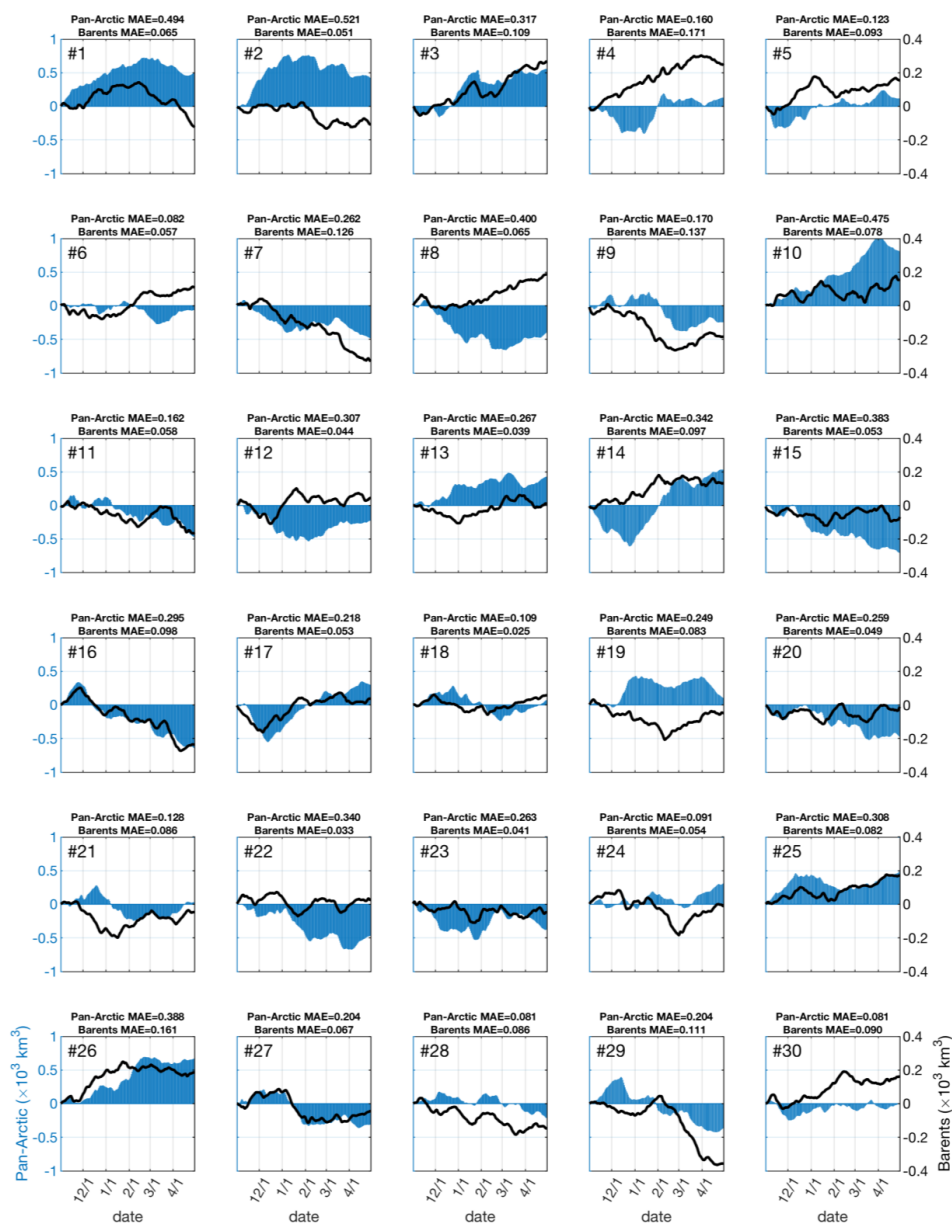
Figure 13. Temporal evolution of mean absolute difference of sea ice volume simulations (10^3 km^3) relative to the ensemble mean for 30 ensemble members of RASM integrations from 1th November 2010 until 30 th April 2020 in forecast mode for the Pan-Arctic domain (Blue) and the BS domain (black lines). Note the different Pan-Arctic (left) and BS (right) y-scales used in the panels.

810
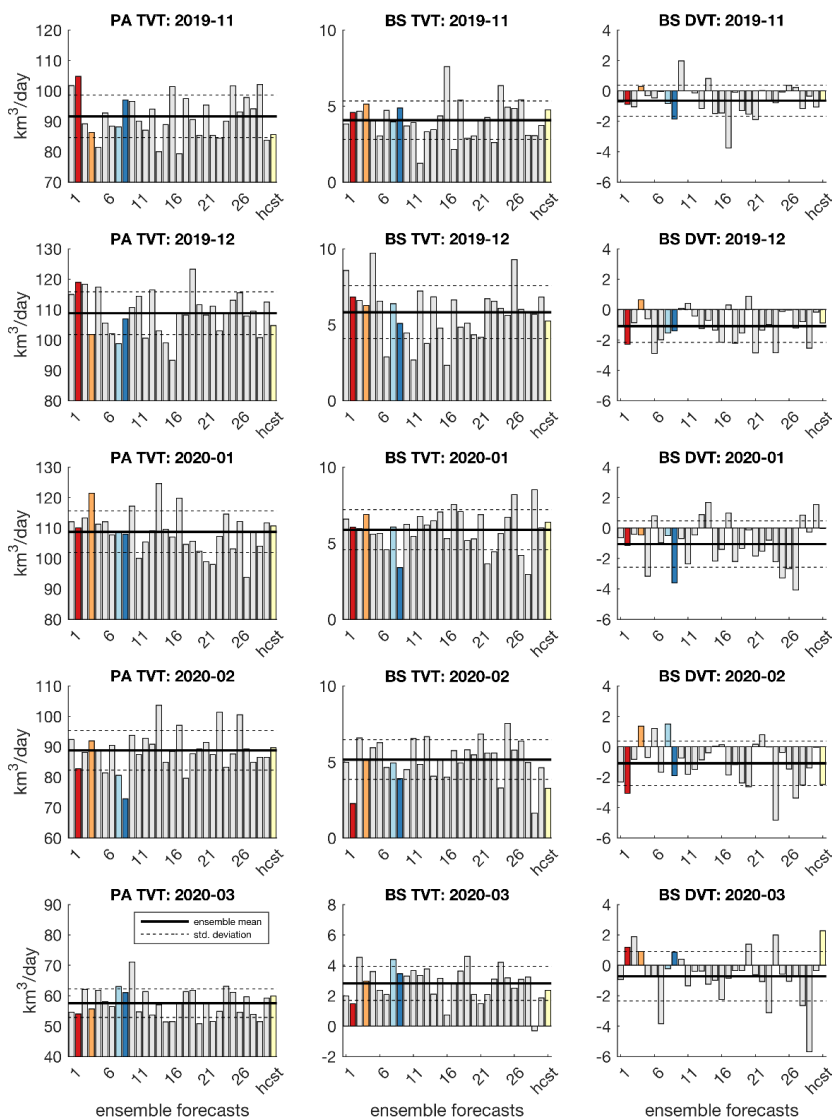
Figure 14. Thermodynamic sea ice volume tendencies (km^3/day) of all 30 ensemble members and the RASM hindcast simulation (yellow) for the Pan-Arctic (left) and the Barents Sea (middle) with the combined ice growth and ice melt terms and the dynamical sea ice volume tendencies (km^3/day) for the Barents Sea (right). Four individual ensemble forecast members are selected and marked as member 2 (red), member 4 (orange), member 8 (light blue) and member 9 (dark blue).

815

820

825

.
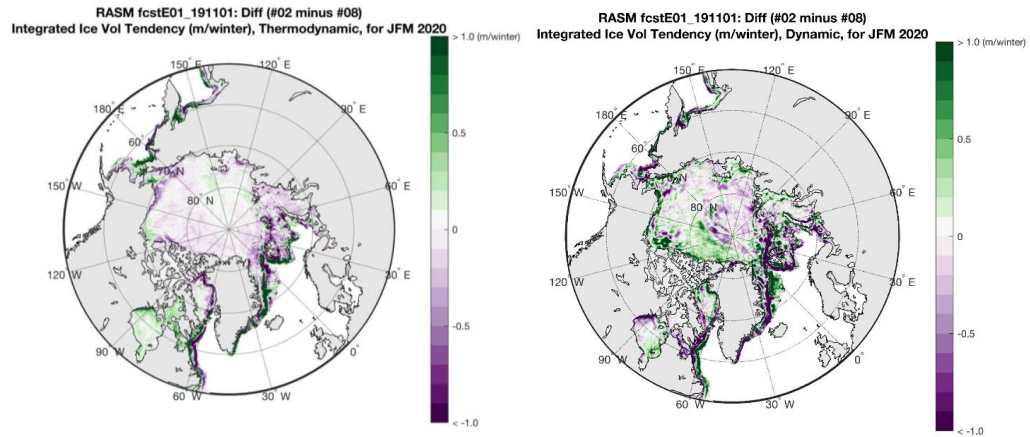
Figure 15. Differences of accumulated thermo-dynamical (m/winter) (left) and dynamical sea ice volume tendencies (m/winter) (right) for JFM 2020 between the RASM ensemble members 2 and 8.

830

835

840

845

850

855
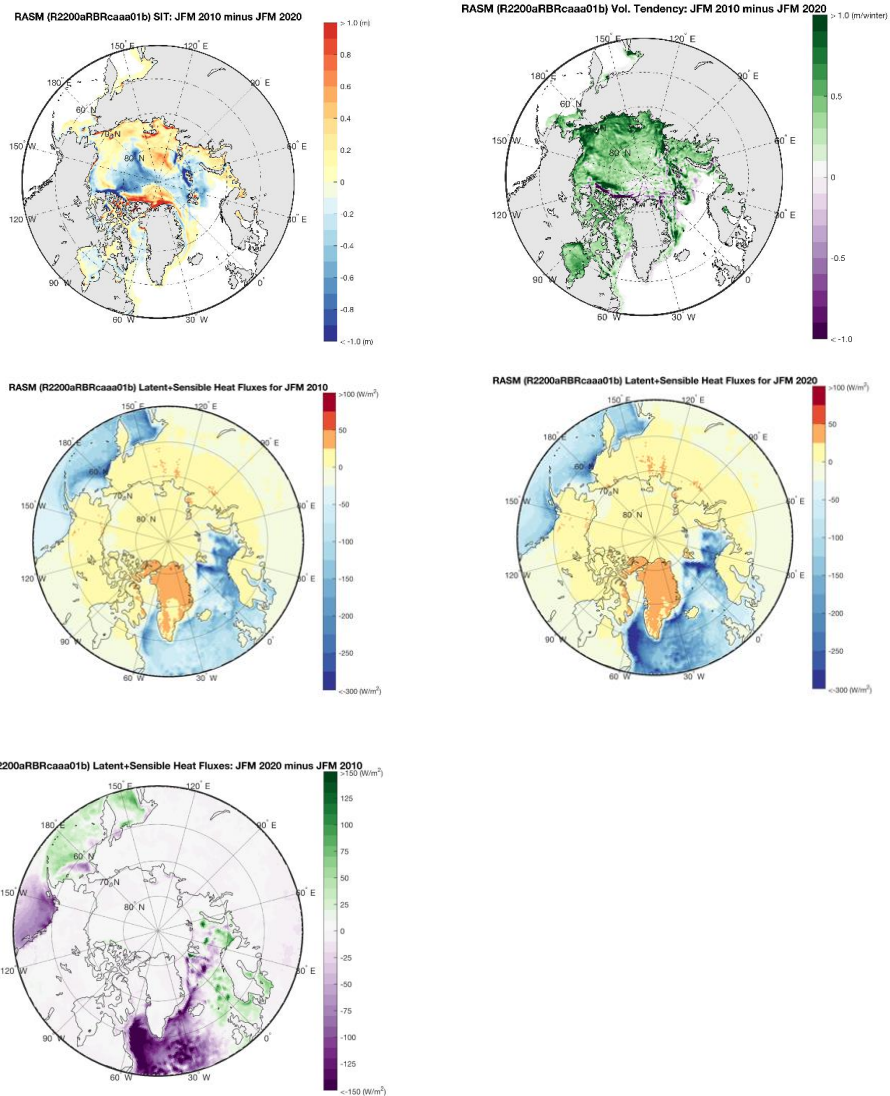
860

Figure 16. The differences of SIT (upper row, left) and total volume tendencies (upper row, right) "JFM 2010 minus JFM 2020" and the
mean combined sensible and latent heat fluxes (W/m^2) for JFM 2010 (middle row, left) and for JFM 2020 (middle row, right) and the
differences of the surface heat fluxes "JFM2020 minus JFM 2010" (lower row) from the RASM hindcast simulation. Note that the flux
convention means, that negative fluxes are from the ocean into the atmosphere.

870